

# Quantifying Intrinsic and Extrinsic Contributions to Radial Anisotropy in Tomographic Models

J. K. Magali<sup>1</sup>, T. Bodin<sup>1</sup>, N. Hedjazian<sup>1</sup>, Y. Ricard<sup>1</sup>, Y. Capdeville<sup>2</sup>, E.  
Debayle<sup>1</sup>

<sup>1</sup>Univ Lyon, Univ Lyon 1, ENSL, UJM-Saint-Etienne, CNRS, LGL-TPE, F-69622, Villeurbanne, France

<sup>2</sup>Laboratoire de Planétologie et Géodynamique, CNRS, UMR 6112, Université de Nantes, F-44322

Nantes, Cedex 3, France.

## Key Points:

- We propose a theoretical expression that relates the observed radial anisotropy to its intrinsic and extrinsic contributions.
- At wavelengths longer than the scale of deformation patterns, tomography underestimates intrinsic anisotropy due to spatial averaging.
- At shorter wavelengths, tomography overestimates intrinsic anisotropy due to the presence of extrinsic anisotropy.

---

Corresponding author: John Keith Magali, [jkvmagali@gmail.com](mailto:jkvmagali@gmail.com)

15 **Abstract**

16 Seismic anisotropy in the Earth’s mantle inferred from seismic observations is usually  
 17 interpreted in terms of intrinsic anisotropy due to Crystallographic Preferred Ori-  
 18 entation (CPO) of minerals, or extrinsic anisotropy due to Shape Preferred Ori-  
 19 entation (SPO). The coexistence of both contributions confuses the origins of seismic  
 20 anisotropy observed in tomographic models. It is thus essential to discriminate CPO  
 21 from SPO. Homogenization/upscaling theory provides means to achieve this goal. It  
 22 enables computing the effective elastic properties of a heterogeneous medium, as seen  
 23 by long-period waves. In this work, we investigate the effects of upscaling an intrin-  
 24 sically anisotropic and highly heterogeneous Earth’s mantle. We show analytically in  
 25 1-D that the observed radial anisotropy parameter  $\xi^*$  is approximately the product of  
 26 the intrinsic  $\xi_{\text{CPO}}^*$  and the extrinsic  $\xi_{\text{SPO}}^*$  components:

27 
$$\xi^* \approx \xi_{\text{CPO}}^* \times \xi_{\text{SPO}}^*,$$

28 when the correlation between the isotropic and anisotropic heterogeneities are ne-  
 29 glected. This law is verified numerically in the case of a homogenized 2-D marble  
 30 cake model of the mantle in the presence of CPO obtained from a micro-mechanical  
 31 model of olivine deformation. Our numerical findings predict that for wavelengths  
 32 smaller than the scale of deformation patterns, tomography may overestimate intrin-  
 33 sic anisotropy due to significant extrinsic anisotropy. At longer wavelengths, intrinsic  
 34 anisotropy is always underestimated due to spatial averaging. Therefore, we show that  
 35 it is imperative to homogenize a CPO evolution model first before drawing compar-  
 36 isons with tomographic models. As a demonstration, we use our composite law with  
 37 a homogenized CPO model of a plate-driven flow underneath a mid-ocean ridge, to  
 38 estimate the SPO contribution to an existing tomographic model of radial anisotropy.

39 **Plain Language Summary**

40 Small-scale heterogeneities may generate long-period seismic observations that  
 41 are identical to those produced by large-scale mantle flow and deformation. Because  
 42 of this, it is difficult to distinguish in the observed seismic anisotropy what is related to  
 43 the intrinsic crystalline anisotropy and what may be due to the laminated structure of  
 44 isotropic materials. In this work, we undertook an analytical method and a numerical  
 45 experiment to identify the separate effects of intrinsic and apparent anisotropy in a  
 46 long wave-length tomographic image. We show that the ambiguity depends on the

47 relation between the wavelength of the observed wavefield and the scale of convection  
48 patterns in the mantle. This motivated us to develop a simple composite law that can  
49 be used to quantify the two separate contributions.

## 50 **1 Introduction**

51 Seismic anisotropy in the Earth’s mantle originates from various processes and  
52 can be observed at different spatial scales (Kendall, 2000; Hansen et al., 2021). At  
53 the mineral scale, crystallographic preferred orientation (CPO) of anisotropic mantle  
54 minerals due to progressive shearing over time produces large-scale intrinsic anisotropy  
55 (Nicolas & Christensen, 1987; Maupin & Park, 2015). On the other hand, rock-scale  
56 shape preferred orientation (SPO) such as layered heterogeneous materials, seismic  
57 discontinuities, preferentially-oriented cracks or conduits containing fluid intrusions  
58 unresolved by long-period seismic waves are mapped as large-scale extrinsic anisotropy  
59 (Backus, 1962; Crampin & Booth, 1985).

60 Although these two mechanisms are completely different, a medium may be ei-  
61 ther (or both) intrinsically anisotropic and extrinsically anisotropic at a given scale,  
62 depending on the minimum wavelength of the observed wavefield used (Maupin et al.,  
63 2007; Wang et al., 2013; Fichtner et al., 2013a; Bodin et al., 2015). Backus (1962)  
64 showed that a horizontally-layered isotropic medium is equivalent to a homogeneous  
65 radially anisotropic medium with a vertical axis of symmetry when sampled by seis-  
66 mic waves whose wavelength is much longer than the thickness of layers. This urged  
67 seismologists to interpret tomographic models separately depending on the type of  
68 data used (*i.e.*, different data-types sample different length scales). Scattering studies  
69 use high frequency body waves and interpret small-scale isotropic heterogeneities in  
70 terms of phase changes (e.g. Tauzin & Ricard, 2014) or chemical stratification (e.g.  
71 Tauzin et al., 2016). On the other hand, long-period surface waves with typical wave-  
72 lengths of the order  $10^2$  km retrieve a smooth anisotropic mantle with scales consistent  
73 with convective flow (e.g. Beghein et al., 2010; Debayle & Ricard, 2013; Bodin et al.,  
74 2015; Maupin & Park, 2015). Surface waves however lack the resolving power to re-  
75 cover sharp seismic discontinuities and instead, map these as long wavelength radial  
76 anisotropy (Backus, 1962; Capdeville et al., 2013). The ambiguity on the origin of  
77 observed anisotropy (*i.e.* whether a material is intrinsically anisotropic or strongly het-

78 erogeneous) may mislead seismologists in interpreting the structural origin of seismic  
 79 anisotropy observed in tomographic images.

### 80 **1.1 Intrinsic anisotropy due to Crystallographic Preferred Orientation**

81 Intrinsic anisotropy results from the preferred alignment of anisotropic crystals  
 82 in an aggregate when subjected to a macroscopic deformation. In the mantle, single  
 83 crystal olivine exhibits orthorhombicity, and hence suffers variations in fast and slow  
 84 P- and S-wave velocities up to 20 % (Kumazawa & Anderson, 1969). When olivine  
 85 and pyroxene form a polycrystalline aggregate and are subsequently deformed in the  
 86 mantle flow, their CPO can be described at first order in terms of a hexagonally  
 87 symmetric medium (e.g. Montagner & Nataf, 1988).

88 Observations of large-scale anisotropy in tomographic models appear to be ubiq-  
 89 uitous in regions associated with strong deformation, and have often been interpreted  
 90 in terms of convective flow (McKenzie, 1979; Long, 2013). For instance, tomographic  
 91 imaging has revealed the presence of strong azimuthal and radial anisotropy in the  
 92 upper  $\sim 250$  km of the mantle (refer to Long and Becker (2010) for a comprehensive  
 93 review). Long wavelength seismic anisotropy is also prevalent in the transition zone  
 94 (e.g. Trampert & van Heijst, 2002; Wookey & Kendall, 2004) although its origin is still  
 95 highly debated (Chen & Brudzinski, 2003; Chang & Ferreira, 2019; Sturgeon et al.,  
 96 2019). Probing deeper depths, the lower mantle appears to be isotropic (e.g. Meade et  
 97 al., 1995) barring the D" layer where enough evidence have shown it to be anisotropic  
 98 (e.g. Kendall & Silver, 1998; McNamara et al., 2002; Beghein et al., 2006; Panning &  
 99 Romanowicz, 2006).

100 Since CPO maps the deformation patterns, CPO may deviate from the flow  
 101 direction. This is because the deformation patterns relate not to the velocity field itself,  
 102 but to the velocity gradient. Moreover, CPO is not instantaneous, but depends on the  
 103 history of the deformation. As a result, regions with short deformation trajectories  
 104 such as beneath mid-ocean ridges appear to have under-developed CPO, and would  
 105 lag behind the direction of shear deformation (Kaminski & Ribe, 2002).

106 Based on laboratory experiments of simple shear, the fast axis of olivine tends  
 107 to align parallel to the long axis of the finite strain ellipsoid (FSE) at low strains due  
 108 to plastic deformation (Zhang & Karato, 1995). At larger strains, dynamic recryst-

109 tallization facilitates the alignment of the olivine fast axis towards the direction of  
110 shear (Zhang & Karato, 1995; Bystricky et al., 2000). Mechanical models of CPO  
111 evolution, coupled with geodynamic flow modeling have been developed to replicate  
112 these results and have been extrapolated at scales consistent with mantle deformation  
113 patterns. Among these is the viscoplastic self-consistent (VPSC) model which is used  
114 to explain the mechanical response of polycrystals to plastic deformation (Tommasi et  
115 al., 2000). Such tools however are computationally expensive, especially when applied  
116 to 3-D and non-steady state flows (Lev & Hager, 2008). Another well-received method  
117 is the D-Rex model, that utilizes a simple kinematic approach (Kaminski et al., 2004).  
118 The predicted CPO is then converted to an elastic medium in which seismic waves can  
119 propagate, and may explain anisotropic signatures observed in seismic data recorded  
120 at the surface.

## 121 **1.2 Extrinsic anisotropy due to Shape Preferred Orientation**

122 Extrinsic anisotropy is observed under two conditions: (1) when the scale of the  
123 heterogeneities is much smaller than the minimum wavelength of the observed wave-  
124 field, and (2) when the contrast between seismic wave velocities (*i.e.* the amplitude of  
125 heterogeneities) is large.

126 One of the known configurations at which extrinsic anisotropy is produced is rock-  
127 scale shape preferred orientation (SPO). In the Earth's mantle, rock-scale SPO can  
128 be the result of igneous differentiation, or more generally of the stirring of chemical  
129 heterogeneities by tectonic or convective deformation (e.g. Faccenda et al., 2019).  
130 Since magmatically differentiated oceanic lithosphere is composed of a basaltic crustal  
131 layer blanketed by a depleted harzburgitic mantle (Allègre & Turcotte, 1986), mantle  
132 structure is often modeled in terms of a mechanical mixture of these two end-member  
133 compositions (e.g. Hofmann, 1988; Xu et al., 2008; Ballmer et al., 2015).

134 Large-scale thermal convection in the mantle triggers the constant injection of  
135 oceanic lithosphere into the mantle (Coltice & Ricard, 1999). It then mechanically  
136 stirs with the surrounding mantle and experiences a series of stretching and thinning  
137 due to the normal and shear strains associated with convection (Allègre & Turcotte,  
138 1986). This led Allègre and Turcotte (1986) to develop a geodynamic model of the  
139 mantle that would depict marble cake-like patterns. In their model, the layering may

140 be erased either by dissolution processes when the stripes become thin enough that  
 141 chemical diffusion becomes efficient, or by mantle reprocessing at mid-ocean ridges.  
 142 Assuming that the mixing preserves the physical properties of the two-end members  
 143 with depth and over geological time scales, such processes may explain rock-scale seis-  
 144 mic heterogeneities observed in the mantle in agreement with the spectrum of isotropic  
 145 anomalies observed along ridges (Agraniier et al., 2005; Xu et al., 2008; Stixrude &  
 146 Jeanloz, 2015).

### 147 **1.3 Long-Period Tomography**

148 There are a plethora of ways to extract interpretable information from seismic  
 149 data. Tomographic imaging techniques however are limited by the type of data used  
 150 due to both computational, and theoretical considerations. Long-period tomography  
 151 uses the relatively low-frequency components of a seismogram such as low-frequency  
 152 travel time residuals, surface wave data, and normal-mode spectral measurements (e.g.  
 153 T. G. Masters et al., 1996; Resovsky & Ritzwoller, 1999) to image mantle structure.  
 154 In practice, they are primarily used to invert for absolute  $V_S$  structures and  $S$ -wave  
 155 anisotropy (e.g. Gung et al., 2003; Panning & Romanowicz, 2006; French et al.,  
 156 2013), although some studies have already documented the use of similar techniques  
 157 to reconstruct  $V_P$  structures (e.g. G. Masters et al., 2000; Koelemeijer et al., 2016).

158 In the context of inversion for radial anisotropy, long-period tomography fails to  
 159 distinguish between an intrinsic or an extrinsic origin. For instance, some tomographic  
 160 models of radial anisotropy inferred from surface wave inversions cannot be explained  
 161 with mineralogical models alone. These profiles of radial anisotropy are instead partly  
 162 interpreted as unmapped small-scales either due to fine-layering, or by sharp gradients  
 163 of lateral heterogeneities (e.g. Schlue & Knopoff, 1977; Montagner & Jobert, 1988;  
 164 Friederich & Huang, 1996; Debayle & Kennett, 2000; Kawakatsu et al., 2009).

165 Indeed, the scale of these heterogeneities are far smaller in comparison with the  
 166 wavefield considered in long-period tomography, and for this reason, the small-scales  
 167 are being mapped as extrinsic anisotropy. Anisotropic structures retrieved from to-  
 168 mography may therefore be a combination of extrinsic anisotropy due to SPO and  
 169 deformation-induced intrinsic anisotropy. However, separating the intrinsic and the  
 170 extrinsic contributions to the observed anisotropy is much difficult in full generality.

171 To simplify the problem, we will focus on quantifying the separate contributions to  
172  $S$ -wave radial anisotropy. This follows most studies that explored the extrinsic con-  
173 tributions to radial anisotropy (Fichtner et al., 2013b; Wang et al., 2013; Bodin et  
174 al., 2015; Alder et al., 2017). Furthermore, we will also ignore the contributions of  
175  $P$ -wave anisotropy which are not well-constrained by long-period tomography, par-  
176 ticularly in the upper-mantle which is mostly constrained by surface waves that have  
177 little sensitivity to  $P$  properties (Takeuchi & Saito, 1972).

178 In this paper, we extend the work of Alder et al. (2017) by estimating the long-  
179 wavelength effective equivalent of a marble cake mantle as hypothesized by Allègre and  
180 Turcotte (1986), but in the presence of intrinsic anisotropy. Our aim is to quantify the  
181 level of effective radial anisotropy resulting from elastic homogenization, that is, the  
182 relegated version of the true Earth as seen by long-wavelength seismic tomography.  
183 Section 2 is a brief overview of the homogenization theory and provides a definition  
184 of some terms and notations to guide the reader throughout the paper. Section 3  
185 shows 1-D analytical expressions for homogenization and highlights a composite law  
186 that separates intrinsic and extrinsic radial anisotropy for a layered and anisotropic  
187 media. Here, we demonstrate that the effective radial anisotropy varies with the  
188 square of isotropic heterogeneities, as well as with the square of anisotropic hetero-  
189 geneities, plus a cross term related to their coupling. In section 4, we build a 2-D  
190 media analogous to the marble cake model where we consider a mechanical mixture of  
191 two end-member compositions. We follow this by introducing intrinsic anisotropy due  
192 to mantle deformation associated with convection patterns consistent with the marble  
193 cake model. We compute the long-wavelength effective equivalent of the 2-D models  
194 using the Fast-Fourier Homogenization algorithm (Capdeville et al., 2015). Section  
195 5 presents the results of the previous section: one of the major findings is that in  
196 the absence of isotropic heterogeneities, intrinsic anisotropy is always underestimated  
197 upon homogenization due to the spatial averaging of the preferred orientation of the  
198 anisotropic minerals. We also verify numerically that the composite law derived in  
199 section 3 can be extended to 2-D media. Finally in section 6, we apply the composite  
200 law to infer the extrinsic component of radial anisotropy from a tomographic model  
201 of the upper-mantle beneath a mid-ocean ridge with the help of a homogenized CPO  
202 model.

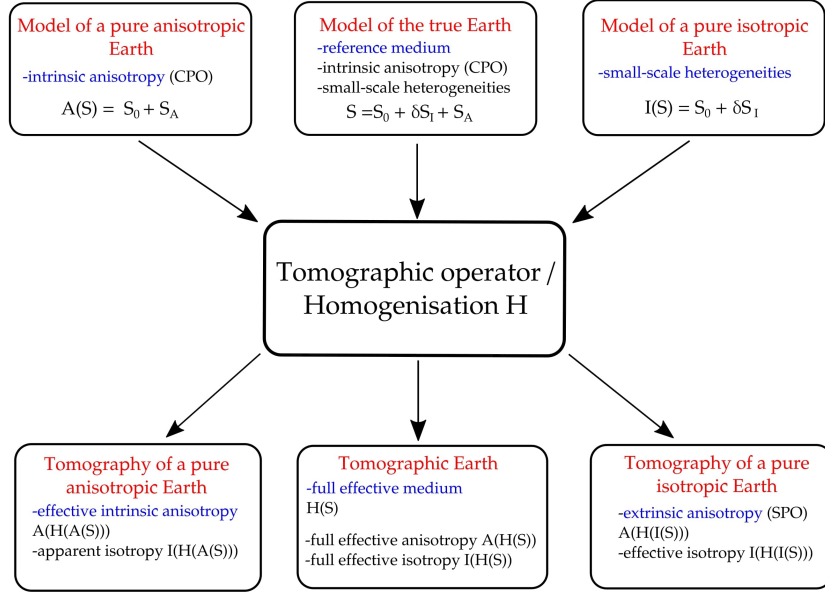


**Figure 1.** Homogenization of different Earth models and their respective outputs. The true Earth mantle (top middle box) is described by an average isotropic model  $S_0$ , isotropic heterogeneities,  $\delta S_I$  and intrinsic anisotropy  $S_A$ , the sum of which being the elastic model  $S$  that tomography tries to recover. However, tomographic methods have only access to a homogenized model  $\mathcal{H}(S)$  (or full effective medium). This model has both isotropic components symbolized by  $\mathcal{I}(\mathcal{H}(S))$  and anisotropic components,  $\mathcal{A}(\mathcal{H}(S))$ . The goal of this paper is to quantify the differences between  $\mathcal{A}(\mathcal{H}(S))$  and  $\mathcal{A}(S)$ ,  $\mathcal{I}(\mathcal{H}(S))$  and  $\mathcal{I}(S)$ . Numerically we can also discuss how an anisotropic model without isotropic heterogeneities (boxes on the left) can be recovered and if the tomographic inversion can lead to apparent isotropic heterogeneities. Reciprocally (boxes on the right), one can quantify how much a pure isotropic model is recovered by the tomographic inversion and what is the level of extrinsic anisotropy (SPO) that can be estimated.

## 203 **2 Elastic homogenization**

204 Even assuming perfect data coverage, seismic tomography is only able to recover  
 205 a smooth representation of the real Earth due to the limited frequency band of seis-  
 206 mic data. This smooth average, however, is not just a simple spatial average but is  
 207 produced from highly non-linear upscaling relations. In the context of wave propaga-  
 208 tion, such upscaling relations, also known as elastic homogenization, remove seismic  
 209 heterogeneities whose scales are much smaller than the minimum wavelength of the  
 210 observed wavefield, and instead replace them with effective properties.



211 Hereafter, what we refer to as the *true elastic structure*  $\mathbf{S}(\mathbf{r})$  is an elastic model  
 212 of the real Earth varying in space  $\mathbf{r}$  that accounts for both intrinsic anisotropy due to  
 213 CPO and small-scale isotropic heterogeneities that resemble marble cake-like patterns.  
 214 One can express  $\mathbf{S}(\mathbf{r})$  in terms of a spatially-varying isotropic tensor  $\mathbf{S}_{\mathbf{I}}(\mathbf{r})$  defined by  
 215 the two Lamé parameters:  $\lambda(\mathbf{r})$  and  $\mu(\mathbf{r})$ , plus an intrinsically-anisotropic component  
 216  $\mathbf{S}_{\mathbf{A}}(\mathbf{r})$  related to CPO:

$$217 \quad \mathbf{S}(\mathbf{r}) = \mathbf{S}_{\mathbf{I}}(\mathbf{r}) + \mathbf{S}_{\mathbf{A}}(\mathbf{r}), \quad (1)$$

218 where  $\mathbf{S}_{\mathbf{I}}(\mathbf{r})$  can be decomposed further into:

$$219 \quad \mathbf{S}_{\mathbf{I}}(\mathbf{r}) = \mathbf{S}_{\mathbf{0}} + \delta\mathbf{S}_{\mathbf{I}}(\mathbf{r}). \quad (2)$$

220 Here,  $\mathbf{S}_{\mathbf{0}}$  is an isotropic tensor uniform in space, and  $\delta\mathbf{S}_{\mathbf{I}}(\mathbf{r})$  is a deviation from  $\mathbf{S}_{\mathbf{0}}$   
 221 related to small-scale isotropic heterogeneities. The true elastic structure becomes:

$$222 \quad \mathbf{S}(\mathbf{r}) = \mathbf{S}_{\mathbf{0}} + \delta\mathbf{S}_{\mathbf{I}}(\mathbf{r}) + \mathbf{S}_{\mathbf{A}}(\mathbf{r}). \quad (3)$$

223 For convenience, let us introduce an operator  $\mathcal{I}$  that extracts the isotropic component  
 224 from  $\mathbf{S}$ , and an operator  $\mathcal{A}$  that extracts the anisotropic component from  $\mathbf{S}$ :

$$225 \quad \begin{aligned} \mathcal{I}(\mathbf{S}(\mathbf{r})) &= \mathbf{S}_{\mathbf{I}}(\mathbf{r}) = \mathbf{S}_{\mathbf{0}} + \delta\mathbf{S}_{\mathbf{I}}(\mathbf{r}) \\ \mathcal{A}(\mathbf{S}(\mathbf{r})) &= \mathbf{S}_{\mathbf{0}} + \mathbf{S}_{\mathbf{A}}(\mathbf{r}), \end{aligned} \quad (4)$$

226 where  $\mathcal{I}$  extracts the isotropic component by first computing the dilatational and Voigt  
 227 stiffness tensors followed by the computation of the bulk and the shear moduli (Cowin  
 228 & Mehrabadi, 1987), and  $\mathcal{A}$  performs similar to the elastic decomposition method of  
 229 Browaeys and Chevrot (2004) where the anisotropic component is treated as a sum of  
 230 orthogonal projections belonging to several symmetry classes.

231 These notations will be used heavily in the rest of the text to denote the isotropic  
 232 and anisotropic components of an elastic medium. Radial anisotropy, in particular,  
 233 quantifies the level of anisotropy when the medium is averaged azimuthally (Montagner,  
 234 2007; Maupin et al., 2007). In such a vertically transverse isotropic medium (VTI),  
 235 the level of  $S$ -wave radial anisotropy is given by  $(V_{SH}/V_{SV})^2$ , where  $V_{SV}$  is the ve-  
 236 locity of vertically traveling  $S$ -waves or horizontally traveling  $S$ -waves with vertical  
 237 polarization, and  $V_{SH}$  is the velocity of horizontally traveling  $S$ -waves with horizontal  
 238 polarization. The *intrinsic  $S$ -wave radial anisotropy* extracted from  $\mathcal{A}(\mathbf{S})$  (*i.e.* due  
 239 to the component  $\mathbf{S}_{\mathbf{A}}$ ) will be denoted by  $\xi_{\text{CPO}}$ .

240 In the event where long-period waves sample the true elastic structure, small-  
 241 scale heterogeneities are seen only through their effective properties. Computing these  
 242 effective properties is designated by a mathematical operator  $\mathcal{H}$  called *upscaling* or  
 243 *homogenization*. Setting aside the imperfections of inversion algorithms and data cov-  
 244 erage, performing seismic tomography can be viewed as applying the operator  $\mathcal{H}$  that  
 245 homogenizes  $\mathbf{S}$ . The seismic tomography model/long-wavelength effective medium of  
 246  $\mathbf{S}$  is then  $\mathcal{H}(\mathbf{S}) = \mathcal{H}(\mathbf{S}_0 + \delta\mathbf{S}_I + \mathbf{S}_A)$  which we now refer to as the *full effective medium*.  
 247 The anisotropic component of the full effective medium given by  $\mathcal{A}(\mathcal{H}(\mathbf{S}))$  will be re-  
 248 ferred hereafter as the *full effective anisotropy* and its isotropic component  $\mathcal{I}(\mathcal{H}(\mathbf{S}))$  is  
 249 the *full effective isotropy*. We will symbolize the *full effective radial anisotropy* corre-  
 250 sponding to  $\mathcal{A}(\mathcal{H}(\mathbf{S}))$  with  $\xi^*$ .

251 On the other hand, the homogenized counterpart of a pure anisotropic Earth  
 252 (*i.e.*, a model where only the anisotropic component varies spatially) is  $\mathcal{H}(\mathcal{A}(\mathbf{S})) =$   
 253  $\mathcal{H}(\mathbf{S}_0 + \mathbf{S}_A)$  where  $\mathcal{A}(\mathcal{H}(\mathcal{A}(\mathbf{S})))$  is the *effective intrinsic anisotropy*. The *effective*  
 254 *intrinsic radial anisotropy* corresponding to  $\mathcal{A}(\mathcal{H}(\mathcal{A}(\mathbf{S})))$  will then be designated as  
 255  $\xi_{\text{CPO}}^*$ . Note that due to the non-linearity of  $\mathcal{H}$ , homogenization creates apparent  
 256 isotropic heterogeneities in the elastic tensor  $\mathcal{I}(\mathcal{H}(\mathcal{A}(\mathbf{S})))$  as a byproduct, albeit of low  
 257 amplitude.

258 Finally, the tomographic counterpart of a pure isotropic Earth (*i.e.*, a model  
 259 where the isotropic component varies spatially, and the anisotropic component is zero)  
 260 is  $\mathcal{H}(\mathcal{I}(\mathbf{S})) = \mathcal{H}(\mathbf{S}_0 + \delta\mathbf{S}_I)$  where the non-negligible apparent anisotropic compo-  
 261 nent due to SPO  $\mathcal{A}(\mathcal{H}(\mathcal{I}(\mathbf{S})))$  is called *extrinsic anisotropy*. Here, *extrinsic radial*  
 262 *anisotropy* will be denoted by  $\xi_{\text{SPO}}^*$  (Refer to Figure 1 for a comprehensive summary).

### 263 **3 Analytical expressions in the 1-D case**

#### 264 **3.1 Backus homogenization**

265 A vertically transverse isotropic (VTI) medium is an elastic medium with hexag-  
 266 onal symmetry and vertical symmetry axis. It can be described by five elastic param-  
 267 eters  $A$ ,  $C$ ,  $F$ ,  $L$ , and  $N$ , also known as the Love parameters (Love, 1906). Supposing  
 268 that axis 3 is the symmetry axis, the local  $\mathbf{S}$  for a VTI solid can be expressed in Mandel

269 notation as:

$$270 \quad \mathbf{S} = \begin{pmatrix} A & A - 2N & F & 0 & 0 & 0 \\ A - 2N & A & F & 0 & 0 & 0 \\ F & F & C & 0 & 0 & 0 \\ 0 & 0 & 0 & 2L & 0 & 0 \\ 0 & 0 & 0 & 0 & 2L & 0 \\ 0 & 0 & 0 & 0 & 0 & 2N \end{pmatrix}. \quad (5)$$

271 In a weakly anisotropic medium, *SV*– and *SH*– waves are sensitive to the elastic  
272 parameters  $L$  and  $N$ , respectively, according to the formula:

$$273 \quad V_{SV} = \sqrt{\frac{L}{\rho}} \quad (6)$$

$$274 \quad V_{SH} = \sqrt{\frac{N}{\rho}}, \quad (7)$$

275 where  $\rho$  is density. The level of *S*–wave radial anisotropy is controlled by the anisotropic  
276 parameter:

$$277 \quad \xi = \left( \frac{V_{SH}}{V_{SV}} \right)^2 = \frac{N}{L}. \quad (8)$$

278 Backus (1962) explicitly showed analytical upscaling relations for seismic waves propa-  
279 gating in a 1-D stratified medium. For a 1-D layered medium where each layer is a VTI  
280 medium, the long-wavelength effective medium is also a VTI medium. The effective  
281 equivalent of the elastic constants, for instance,  $N$  and  $L$  concerning the shear wave  
282 velocities are given by an arithmetic mean and a harmonic mean, respectively:  
283

$$284 \quad N^* = \langle N \rangle, \quad (9)$$

$$285 \quad L^* = \langle 1/L \rangle^{-1}, \quad (10)$$

286 where  $\langle \cdot \rangle$  refers to the spatial average over a wavelength of any periodic function (in  
287 this case,  $N$  and  $1/L$ ), and \* denotes a long wavelength effective property. The effective  
288 density  $\rho^*$  is simply the arithmetic mean of the local density  $\rho$ :  
289

$$290 \quad \rho^* = \langle \rho \rangle. \quad (11)$$

291 The effective *S*–radial anisotropy  $\xi^*$  is essentially the ratio between the effective equiv-  
292 alents of  $N$  and  $L$ :

$$293 \quad \xi^* = \frac{N^*}{L^*} = \langle N \rangle \langle 1/L \rangle. \quad (12)$$

In this way, for a 1-D fine-scale medium where each layer is isotropic ( $N = L$ ), the long-wavelength effective medium is transversely isotropic, and the level of extrinsic radial anisotropy is given by  $\langle N \rangle \langle 1/N \rangle$  (Alder et al., 2017).

### 3.2 An analytical expression to quantify CPO and SPO in a 1-D layered media

Let us consider an intrinsically anisotropic (CPO component) and finely-layered (SPO component) 1-D VTI medium. Assuming in the matrix (5), no  $P$ -wave anisotropy (*i.e.*,  $C = A$ ) and setting  $F = A - 2L$ , one can express the isotropic rigidity as (Montagner, 2007; Maupin et al., 2007):

$$\mu = \frac{1}{3}(2L + N). \quad (13)$$

Knowing equations (8) and (13), one can re-write  $N$  and  $L$  in terms of  $\mu$  and  $\xi_{\text{CPO}} = N/L$  giving:

$$N = \xi_{\text{CPO}} \frac{3\mu}{2 + \xi_{\text{CPO}}}, \quad (14)$$

$$L = \frac{3\mu}{2 + \xi_{\text{CPO}}}. \quad (15)$$

To calculate the long-wavelength effective equivalent of such a medium, let us first write the parameters  $\mu$  and  $\xi_{\text{CPO}}$  as:

$$\mu(z) = \langle \mu \rangle + \delta\mu(z), \quad (16)$$

$$\xi_{\text{CPO}}(z) = \langle \xi_{\text{CPO}} \rangle + \delta\xi_{\text{CPO}}(z), \quad (17)$$

where  $\langle \mu \rangle$  and  $\langle \xi_{\text{CPO}} \rangle$  are the spatially-averaged counterparts.  $\delta\mu$  and  $\delta\xi_{\text{CPO}}$  are small-scale radial heterogeneities (*i.e.*, layering) in the shear modulus and intrinsic radial anisotropy, respectively, where  $\langle \delta\mu \rangle$  and  $\langle \delta\xi_{\text{CPO}} \rangle = 0$ .

The long-wavelength effective equivalents  $N^*$  and  $1/L^*$  are:

$$N^* = \langle N \rangle = \left\langle \xi_{\text{CPO}} \frac{3\mu}{2 + \xi_{\text{CPO}}} \right\rangle = \left\langle \left( \langle \xi_{\text{CPO}} \rangle + \delta\xi_{\text{CPO}} \right) \frac{3(\langle \mu \rangle + \delta\mu)}{2 + \langle \xi_{\text{CPO}} \rangle + \delta\xi_{\text{CPO}}} \right\rangle, \quad (18)$$

$$1/L^* = \langle 1/L \rangle = \left\langle \frac{2 + \xi_{\text{CPO}}}{3\mu} \right\rangle = \left\langle \frac{2 + \langle \xi_{\text{CPO}} \rangle + \delta\xi_{\text{CPO}}}{3(\langle \mu \rangle + \delta\mu)} \right\rangle. \quad (19)$$

We can simplify equations (18) and (19) by assuming a weak contrast in the shear modulus  $\delta\mu \ll \langle \mu \rangle$ . Using a second-order Taylor expansion, we get:

$$N^* \approx \frac{3\langle \mu \rangle}{2 + \langle \xi_{\text{CPO}} \rangle} \left( \langle \xi_{\text{CPO}} \rangle - \frac{2\langle \delta\xi_{\text{CPO}}^2 \rangle}{(2 + \langle \xi_{\text{CPO}} \rangle)^2} + \frac{2\langle \delta\mu \cdot \delta\xi_{\text{CPO}} \rangle}{\langle \mu \rangle(2 + \langle \xi_{\text{CPO}} \rangle)} \right), \quad (20)$$

$$1/L^* \approx \frac{2 + \langle \xi_{\text{CPO}} \rangle}{3\langle \mu \rangle} \left( 1 + \frac{\langle \delta\mu^2 \rangle}{\langle \mu \rangle^2} - \frac{\langle \delta\mu \cdot \delta\xi_{\text{CPO}} \rangle}{\langle \mu \rangle(2 + \langle \xi_{\text{CPO}} \rangle)} \right). \quad (21)$$

326 Note that we have used a parameter which is  $\langle \xi_{\text{CPO}} \rangle = 1$  in the absence of intrinsic  
 327 anisotropy in all layers. We could have used, instead, a parameter that cancels in  
 328 the absence of intrinsic anisotropy, for example, the fractional change in shear wave  
 329 velocities  $\gamma = (V_{SH} - V_{SV})/V_S$  (e.g. Xie et al., 2013, 2017). This parameter is also  
 330 used in the Thomsen notation (Thomsen, 1986; Bakulin, 2003) but the two parameters  
 331 are simply related by  $\gamma = 1 - \sqrt{\xi}$ . We decide to keep  $\xi$  since this is the parameter that  
 332 is most often used to observe large-scale mantle anisotropy.

333 Using equation (12), we multiply equations (20) and (21) and neglect terms  
 334 higher than order two to obtain the full effective radial anisotropy  $\xi^*$  due to both  
 335 fine-layering and intrinsic radial anisotropy:

$$336 \quad \xi^* \approx \langle \xi_{\text{CPO}} \rangle - \frac{2}{(2 + \langle \xi_{\text{CPO}} \rangle)^2} \langle \delta \xi_{\text{CPO}}^2 \rangle + \frac{\langle \xi_{\text{CPO}} \rangle}{\langle \mu \rangle^2} \langle \delta \mu^2 \rangle + \frac{2 - \langle \xi_{\text{CPO}} \rangle}{\langle \mu \rangle (2 + \langle \xi_{\text{CPO}} \rangle)} \langle \delta \mu \cdot \delta \xi_{\text{CPO}} \rangle. \quad (22)$$

337 Equation (22) explicitly shows the separate effects of the small-scales in the isotropic  
 338 component and in the intrinsically anisotropic component onto the effective radial  
 339 anisotropy as 'seen' by long-period seismic waves.

340 Assuming the medium to be devoid of intrinsic radial anisotropy (*i.e.*,  $\xi_{\text{CPO}} = 1$   
 341 and  $\delta \xi_{\text{CPO}} = 0$ ), the full effective radial anisotropy  $\xi^*$  directly relates to the variance  
 342 of small-scale heterogeneities  $\langle \delta \mu^2 \rangle$  in the shear modulus  $\delta \mu$ . It can be interpreted  
 343 as the extrinsic radial anisotropy  $\xi_{\text{SPO}}^*$  due to the seismically unresolved small-scale  
 344 isotropic heterogeneities. It varies as the square of the heterogeneities, in agreement  
 345 with the result of Alder et al. (2017).

346 On the other hand, when the isotropic component is uniform (*i.e.*,  $\delta \mu = 0$ ),  $\xi^*$   
 347 also varies with the square of heterogeneities, but now in intrinsic radial anisotropy.  
 348 This can be interpreted as the effective intrinsic radial anisotropy  $\xi_{\text{CPO}}^*$ , *i.e.* the in-  
 349 trinsic radial anisotropy that gets smoothed out as a result of upscaling. Interestingly,  
 350 its overall effect is to reduce the level of intrinsic radial anisotropy as indicated by the  
 351 minus sign in front of the second term. In the absence of small-scale isotropic hetero-  
 352 geneities, we anticipate radial anisotropy to be always underestimated by tomography.

353 Finally, equation (22) suggests the existence of a cross-term  $\langle \delta \mu \cdot \delta \xi_{\text{CPO}} \rangle$  due to  
 354 the spatial correlation between intrinsic radial anisotropy and shear modulus. Sup-  
 355 posing spatial variations in both components are significant such as at major seismic

356 discontinuities, the correlation term should influence the anisotropy mapped in tomo-  
 357 graphic models.

358 Similarly, the effective Voigt-averaged shear modulus  $\mu^*$  is given by:

$$359 \quad \mu^* = \frac{2L^* + N^*}{3}. \quad (23)$$

360 Plugging equations (20) and (21) into equation (23), we get:

$$361 \quad \mu^* = \langle \mu \rangle - \frac{2}{\langle \mu \rangle (2 + \langle \xi_{\text{CPO}} \rangle)} \langle \delta \mu^2 \rangle - \frac{2 \langle \mu \rangle}{(2 + \langle \xi_{\text{CPO}} \rangle)^3} \langle \delta \xi_{\text{CPO}}^2 \rangle + \frac{4}{(2 + \langle \xi_{\text{CPO}} \rangle)^2} \langle \delta \mu \cdot \delta \xi_{\text{CPO}} \rangle. \quad (24)$$

362 Ignoring intrinsic radial anisotropy (*i.e.*,  $\xi_{\text{CPO}} = 1$  and  $\delta \xi_{\text{CPO}} = 0$ ), the effective shear  
 363 modulus  $\mu^*$  is always smaller than its spatially-averaged version  $\langle \mu \rangle$ . Such a result  
 364 is logical in the 1-D case. Here, radial anisotropy induced by fine-layering is always  
 365 positive (equation (22)) thereby having  $N^* > L^*$ . Since  $L$  'counts' twice and  $N$  once in  
 366 its isotropic average, its long-wavelength effective equivalent  $\mu^*$  is always slower than  
 367  $\langle \mu \rangle$ . Contrastingly, if one neglects isotropic heterogeneities and only consider variations  
 368 in intrinsic radial anisotropy, homogenization also results in the underestimation of  
 369 the shear modulus. One would predict that homogenization leads to the creation of  
 370 apparent isotropic heterogeneities due to small-scale variations in CPO. Lastly and  
 371 as expected, the cross term recurs due to the spatial correlation between the shear  
 372 modulus and intrinsic radial anisotropy.

373 Although the homogenized equations (22) and (24) make clear that homogeniza-  
 374 tion leads to correction terms that are only second-order, these effects may not be  
 375 negligible. First, the equations that we obtained are also valid in situations where  
 376  $\langle \xi_{\text{CPO}} \rangle = 1$  but where  $\langle \delta \xi_{\text{CPO}}^2 \rangle$ ,  $\langle \delta \mu^2 \rangle$ , or  $\langle \delta \xi_{\text{CPO}} \delta \mu \rangle$  are different from zero, in which  
 377 case, all observed anisotropy would be related to second order effects. In the case  
 378 of SPO, the variance in the shear modulus  $\mu$  can be extreme in the presence of par-  
 379 tial melt or water in the mantle (e.g Hacker et al., 2003; Auer et al., 2015) . An  
 380 increase in seismic wavespeed variations of about 20% underneath mantle wedges can  
 381 result from the full hydration of periodotite and eclogite (Hacker et al., 2003). This  
 382 may then significantly contribute to the effective radial anisotropy mapped in tomo-  
 383 graphic images. Contrastingly, significant second-order effects due to CPO-related  
 384 radial anisotropy may only be possible if there are relatively fast spatial variations  
 385 in intrinsic anisotropy. For instance, parts of the lithosphere, especially underneath  
 386 oceanic basins, may harbor layering that is composed of frozen-in CPO transported

387 from the ridge (Becker et al., 2008; Hansen et al., 2016; Hedjazian et al., 2017) and  
 388 the isotropic mantle lithosphere. This layering may produce sharp spatial variations  
 389 in intrinsic radial anisotropy. According to equation (22), this would tone down the  
 390 level of the observed radial anisotropy.

391 The homogenized expressions given by equations (22) and (24) in terms of the  
 392 isotropic shear modulus  $\mu$  may not be particularly convenient for seismologists. In  
 393 practice, spatial distributions in  $V_S$ , and not in  $\mu$ , are observed. If one assumes that  
 394 density is uniform, then  $\delta\mu/\mu$  can be simply replaced by  $2\delta V_S/V_S$ . On the other hand,  
 395 if one assumes that density increases with  $V_S$ , one could also establish long-wavelength  
 396 effective expressions for  $V_S$  in the same manner as  $\mu$  using simple empirical relations  
 397 for density such as that of Tkalcic et al. (2006).

398 In the Earth's asthenosphere where large-scale anisotropy due to mantle deformation  
 399 is prevalent, the expected shear modulus heterogeneities between mineralogical  
 400 phases seem at most 10% (e.g. Xu et al., 2008; Stixrude & Jeanloz, 2015). To perform  
 401 a numerical estimate, let us examine a stack of planar layers with alternating shear  
 402 moduli values differing by 20% (Figure 2a middle panel). The 1-D depth profiles  
 403 depict periodic variations with layers of equal thicknesses of 20 km. Positive intrinsic  
 404 radial anisotropy ( $\xi = 1.2$ ) is prescribed in the even layers, whereas the odd layers  
 405 are isotropic ( $\xi = 1$ ) (Figure 2a right panel). After upscaling over a wavelength much  
 406 larger than 20 km, the resulting profiles for  $N^*$  and  $L^*$  are homogeneous, and simply  
 407 given by their arithmetic and harmonic means, respectively (Figure 2a left panel).  
 408 Once the long-wavelength effective  $N^*$  and  $L^*$  are acquired, we can compute the full  
 409 effective radial anisotropy  $\xi^*$  through equation (12) (solid red line in Figure 2a right  
 410 panel), and the effective shear modulus  $\mu^*$  through equation (23) (solid red line in  
 411 Figure 2a middle panel). Figure 2b illustrates a different scenario where  $\xi$  only exists  
 412 in the odd layers (Figure 2b right panel). In essence when the shear modulus and  
 413 intrinsic radial anisotropy are uncorrelated, the homogenized parameters  $\mu^*$  and  $\xi^*$   
 414 should be the same regardless. However, a slight offset in  $\mu^*$  and  $\xi^*$  of Figure 2b with  
 415 respect to Figure 2a can be observed which is exclusively attributed to this cross term  
 416 as hinted by equations (22) and (24). Strictly speaking, the reduction in the ampli-  
 417 tude of the effective properties arises from the switch in signs in the cross term from  
 418 positive to negative  $\langle\delta\mu \cdot \delta\xi\rangle$ , implying that in the second scenario, the shear modulus  
 419 and intrinsic radial anisotropy are anti-correlated.

420 To validate the second-order approximation, we also show  $\xi^*$  and  $\mu^*$  using equa-  
 421 tions (22) and (24) respectively (dashed blue lines in Figures 2a and 2b middle and  
 422 right panels). Clearly by applying equation (22), the intrinsic component (first term)  
 423 contributes the most to the effective radial anisotropy with  $1 - \langle \xi_{\text{CPO}} \rangle = 0.1$ . Its  
 424 spatial variations' (second term) overall effect is to tone-down the amplitude of ra-  
 425 dial anisotropy by  $\sim 1\%$ . This is followed by the SPO component (third term) which  
 426 is responsible for the amplification of radial anisotropy by  $\sim 10\%$ . Lastly, the cross  
 427 term provides the least contribution (less than  $\pm 1\%$ ) and therefore can reasonably  
 428 be ignored in this case. The  $\pm$  sign denotes that it may increase or decrease radial  
 429 anisotropy depending on the coupling pattern between the shear modulus and intrinsic  
 430 radial anisotropy.

### 431 3.3 Composite law for $S$ -wave radial anisotropy

432 In this section, we show how the effective radial anisotropy can be expressed in  
 433 terms of its intrinsic and extrinsic contributions. For that, we investigate two special  
 434 cases: (1) a purely isotropic 1-D layered medium, (2) an anisotropic 1-D medium  
 435 (*i.e.*, no spatial variations in isotropic component), and find equivalent expressions for  
 436 extrinsic radial anisotropy  $\xi_{\text{SPO}}^*$  and effective intrinsic radial anisotropy  $\xi_{\text{CPO}}^*$ . By doing  
 437 so, we elicit a simple composite law related to equation (22) that can be extrapolated  
 438 to 2-D and 3-D media.

439 In the case of an isotropic medium with spatially-varying shear modulus, the  
 440 radial anisotropy is entirely due to SPO. Equation (22) reforms into:

$$441 \xi_{\text{SPO}}^* \approx 1 + \frac{\langle \delta \mu^2 \rangle}{\langle \mu \rangle^2}. \quad (25)$$

442 On the other hand, an anisotropic medium without spatial variations in the shear  
 443 modulus leads to an effective intrinsic radial anisotropy:

$$444 \xi_{\text{CPO}}^* \approx \langle \xi_{\text{CPO}} \rangle - \frac{2\langle \delta \xi_{\text{CPO}}^2 \rangle}{(2 + \langle \xi_{\text{CPO}} \rangle)^2}. \quad (26)$$

445 By taking the product between equations (25) and (26), neglecting terms higher than  
 446 order two, one has simply:

$$447 \xi_{\text{CPO}}^* \times \xi_{\text{SPO}}^* \approx \langle \xi_{\text{CPO}} \rangle - \frac{2\langle \delta \xi_{\text{CPO}}^2 \rangle}{(2 + \langle \xi_{\text{CPO}} \rangle)^2} + \frac{\langle \xi_{\text{CPO}} \rangle \langle \delta \mu^2 \rangle}{\langle \mu \rangle^2}, \quad (27)$$

448 which is approximately equal to  $\xi^*$  in equation (22) but without the cross term. There-  
 449 fore, ignoring spatial correlations between intrinsic radial anisotropy and shear mod-



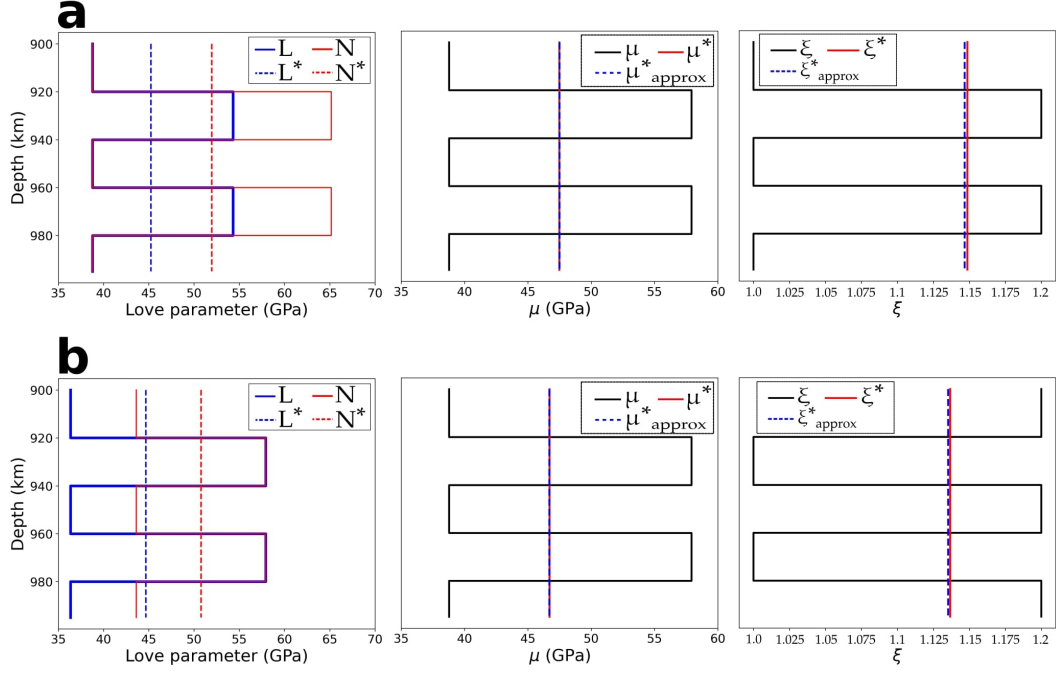


**Figure 2.** 1-D binary and periodic media with 20% isotropic heterogeneities in shear modulus prescribed across: (a) even layers, and (b) odd layers. Upon homogenization, the resulting profiles are homogeneous (variables denoted by (\*)). The dashed blue lines at the middle ( $\mu^*_{\text{approx}}$ ) and right panels ( $\xi^*_{\text{approx}}$ ) correspond to the predicted long-wavelength effective equivalents using the second order approximations from equations (24) and (22), respectively. The difference in the homogenized shear moduli and radial anisotropy between (a) and (b) is attributed to the cross term as implied by equation (22). Since the medium is periodic, it is enough to only display a portion of the medium.

450 ulus, the full effective radial anisotropy can be quantified through the following com-  
 451 posite law:

$$452 \quad \xi^* \approx \xi_{\text{CPO}}^* \times \xi_{\text{SPO}}^*. \quad (28)$$

453 In practice,  $\xi^*$  can be estimated from a tomographic inversion (Debayle & Ken-  
 454 nett, 2000; Plomerová et al., 2002; Gung et al., 2003; Nettles & Dziewoński, 2008a;  
 455 Fichtner et al., 2010). Seismologists often compare  $\xi^*$  with the intrinsic radial anisotropy  
 456  $\xi_{\text{CPO}}$  computed from a geodynamically-based CPO model (Becker et al., 2003, 2006;  
 457 Ferreira et al., 2019; Sturgeon et al., 2019). The comparison should be done instead  
 458 with an effective model  $\xi_{\text{CPO}}^*$ , which is difficult to estimate without access to any  
 459 elastic homogenization tools. Furthermore, equation (22) suggests that there is a non-  
 460 negligible extrinsic component of radial anisotropy due to the unresolved small-scale  
 461 isotropic heterogeneities. While it is difficult to rigorously establish analytical solu-  
 462 tions in the case of a 2-D/3-D complex media, following the logic above, we hypothesize  
 463 that the mismatch often observed between homogenized CPO models and tomographic  
 464 models is the extrinsic radial anisotropy  $\xi_{\text{SPO}}^*$ .

## 465 **4 Methods for 2-D media**

### 466 **4.1 Homogenization in 2-D and in 3-D media**

467 The classic homogenization method of Backus is only applicable in 1-D to media  
 468 exhibiting spatial periodicity. The true Earth, however, is a complex 3-D and multi-  
 469 scale medium. To alleviate this problem and quantify effective elastic properties in  
 470 a mantle-like medium, we rely on the non-periodic elastic homogenization technique  
 471 developed by Capdeville and Marigo (2007); Capdeville et al. (2010); Guillot et al.  
 472 (2010); Capdeville et al. (2015). Originally, this method has been developed as a pre-  
 473 processing step enabling one to solve the elastostatic wave equation using a simple  
 474 mesh, speeding up the computations for wave propagation in complex media. It has  
 475 also been used to improve the convergence and computational cost of full waveform  
 476 inversion (Capdeville & Métivier, 2018; Hedjazian et al., 2021). Most homogenization  
 477 methods rely on a "cell" problem: a set of static elasticity problems whose solutions  
 478 are the base of the effective medium (Sanchez-Palencia, 1980). In the 1-D case, this  
 479 "cell" problem has an analytical solution which leads to explicit formulas for the ef-  
 480 fective medium such as the one found in Backus (1962). In higher dimensions, this

481 analytical solution does not exist and we need to rely on a numerical solver to obtain  
 482 the solutions of the cell problem. Finite element methods are classically used for this  
 483 purpose. Nevertheless, solvers based on the periodic Lippman-Schwinger equation and  
 484 fast Fourier transforms (Moulinec & Suquet, 1998) can also be very efficient leading  
 485 to a mesh-less tool (Capdeville et al., 2015).

486 In the non-periodic case, the homogenization is not performed with respect to the  
 487 periodicity of the medium, but with respect to the minimum wavelength present in the  
 488 wavefield. The assumption that this minimum wavelength  $\lambda_{\min}$  exists is required for  
 489 non-periodic medium with no scale separation such as the true Earth. Scales smaller  
 490 than  $\lambda_{\min}$  are seen by the wavefield only through their effective properties. To sep-  
 491 arate the small and the large scales, we need to define a threshold wavelength  $\lambda_h$ ,  
 492 called the homogenization wavelength.  $\lambda_h$  is a user-defined parameter, and all scales  
 493 smaller than  $\lambda_h$  are homogenized. Numerical examples suggest that, for all natural  
 494 media, homogenization with a value  $\lambda_h = 0.5\lambda_{\min}$  is sufficient to accurately reproduce  
 495 the complete wavefield (Capdeville et al., 2010). Hence, this value is chosen in the  
 496 rest of the present study. Computing the effective properties of an elastic medium  
 497 with homogenization wavelength  $\lambda_h$  requires to solve an elastostatic problem numer-  
 498 ically. To do this, we use the 3-D Fast-Fourier Homogenization algorithm developed  
 499 by Capdeville et al. (2015).

500 In practice, two factors prevent the recovery of the true Earth by tomographic  
 501 methods: (1) limited frequency band of the recorded seismic signals, and (2) limited  
 502 data coverage of ray paths. In the context of full-waveform inversions with perfect  
 503 coverage (*i.e.*, where sources and receivers are densely distributed at the surface of the  
 504 volume to image), Capdeville and Métivier (2018) numerically verified that a seismic  
 505 tomography model and the homogenized model are in agreement at spatial wavelengths  
 506 higher than  $\lambda_h$ . Hence, homogenization can be viewed as a first-order tomographic  
 507 operator assuming perfect data coverage. We will consider the homogenized model as  
 508 the best image one could get from seismic tomography. This can be translated to:

$$509 \quad \mathbf{S}^* = \mathcal{H}(\mathbf{S}) \quad (29)$$

510 where  $\mathcal{H}$  is the tomographic operator,  $\mathbf{S}$  is the true elastic structure, and the homoge-  
 511 nized model  $\mathbf{S}^*$  is the full effective medium (*i.e.*, the best recovered image as seen by a  
 512 wavefield of a given minimum wavelength  $\lambda_{\min}$  and assuming perfect data coverage).

513 In this paper, we apply this 'tomographic operator' to a 2-D composite medium by  
 514 upscaling the marble cake model in the presence of deformation-induced anisotropy.  
 515 Note that the effect of limited data coverage could be simply accounted for by apply-  
 516 ing the tomography resolution matrix to  $\mathbf{S}^*$  (Simmons et al., 2019). For simplicity, we  
 517 ignore this effect in this work.

## 518 4.2 Isotropic heterogeneities in a 2-D mechanically-mixed mantle

519 To define our 2-D incompressible flow model imitating mantle convection, we use  
 520 a stream function similar to that of Alder et al. (2017):

$$521 \quad \Psi(x, z, t) = \sin(a\pi z) [\sin(b\pi x) + \alpha(t) \sin((b+1)\pi x) + \beta(t) \sin((b+2)\pi x)] \quad (30)$$

522 where  $\alpha(t)$  and  $\beta(t)$  are sinusoidal functions of time that introduces chaotic mixing.  
 523 The variables  $a$  and  $b$  relate to the number of distinguishable convection cells and are  
 524 chosen arbitrarily. The form of the function  $\Psi$  ensures free-slip boundary conditions.  
 525 Finally, the resulting velocity field is scaled using a reference value of  $1 \text{ cm}\cdot\text{yr}^{-1}$ .

526 We replicate the marble cake patterns by deforming a circular anomaly at the  
 527 center of the box using our prescribed flow field. To do this, control points that define  
 528 the contour of the anomaly are advected using fourth-order Runge Kutta methods  
 529 with variable time-stepping (Press et al., 1992). To achieve a final configuration for the  
 530 anomaly, we define an advection mixing time  $T_{\text{SPO}}$ . Figure 3 illustrates the evolution  
 531 of the pattern when subjected to the flow field defined in equation (30). Setting  
 532  $a = 1$ ,  $b = 2$ , and  $T_{\text{SPO}} = 75 \text{ My}$ , we have a mechanically-mixed medium with two  
 533 characteristic convection cells.

534 Using the last panel of Figure 3, the binary system is defined by assigning a  
 535 reference S-wave velocity value  $V_{S_2} = 4.52 \text{ km}\cdot\text{s}^{-1}$  to the yellow region, and  $V_{S_1} =$   
 536  $3.7 \text{ km}\cdot\text{s}^{-1}$  to the purple region so that the level of isotropic heterogeneities is given  
 537 by  $100\% \times (V_{S_1} - V_{S_2}) / (V_{S_1} + V_{S_2}) = 10\%$ .  $P$ -wave velocities are computed by  
 538 imposing a constant ratio  $V_P/V_S = 1.7$  (Obrebski et al., 2010). Following the work  
 539 of Tkalčić et al. (2006), we compute the density  $\rho$  using the empirical relation  $\rho =$   
 540  $2.35 + 0.036(V_P - 3)^2$ . These values are used to define the local isotropic tensor  $\mathbf{S}_{\mathbf{I}}$  in  
 541 equation (1).

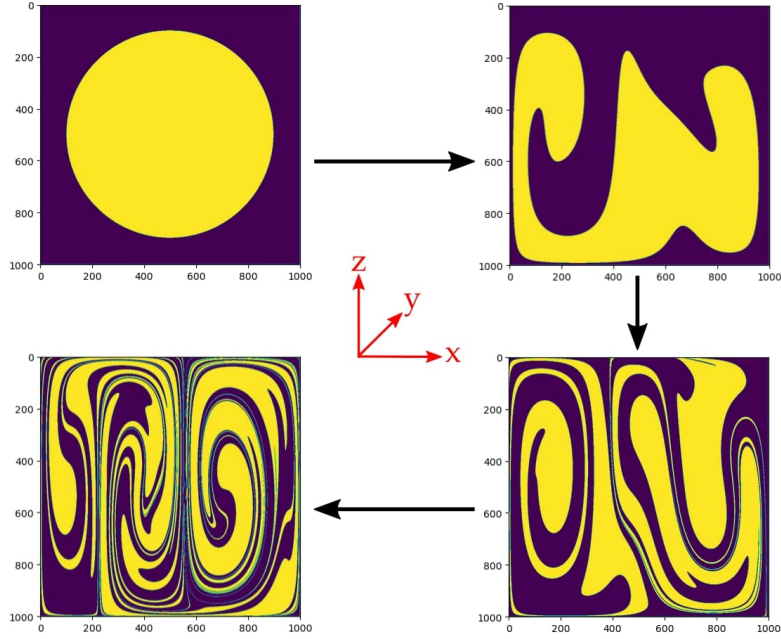


**Figure 3.** Initially a circle, the anomaly is deformed progressively until the medium reaches a stage resembling marble cake-like patterns.

542

### 4.3 Modeling of Crystallographic Preferred Orientation

543

544

545

546

547

548

549

Using the velocity gradient tensor derived from the stream function  $\Psi$  described previously, we then model CPO evolution of olivine aggregates using **D-Rex**, a program that calculates strain-induced CPO by plastic deformation, and dynamic recrystallization (Kaminski et al., 2004). The activities of olivine slip systems are chosen to correspond to dry mantle conditions, while other parameters are taken as in the reference **D-Rex** model. To control the level of intrinsic anisotropy, we assume that CPO only developed in the last  $T_{CPO}$  of the simulation.

550

551

552

553

554

555

In our numerical experiments, we compute CPO everywhere irrespective of the actual mineralogical phase. We scale the elastic tensor derived from **D-Rex** so that its isotropic component is identical to the binary system derived in Section 4.2. The true elastic structure can be constructed from equation (1) where  $\mathbf{S}_I$  now relates to the small-scale isotropic heterogeneities in the mechanically-mixed mantle, and  $\mathbf{S}_A$  is the intrinsically anisotropic component computed with **D-Rex**.

#### 556 4.4 Quantifying the level of anisotropy

557 In this section, we define two ways to quantify the level of seismic anisotropy  
 558 for any given elastic tensor  $\mathbf{S}$ . The first one is radial anisotropy. We project the  
 559 elastic tensor in terms of an azimuthally-averaged vertically transverse isotropic (VTI)  
 560 medium to obtain a tensor described as in equation (5). Here, the parameters  $L$  and  
 561  $N$  can be computed from  $\mathbf{S}$  as follows (Montagner & Nataf, 1986):

$$562 \quad L = \frac{1}{2}(S_{44} + S_{55}) \quad (31)$$

$$563 \quad N = \frac{1}{8}(S_{11} + S_{22}) - \frac{1}{4}S_{12} + \frac{1}{2}S_{66}. \quad (32)$$

565 The level of radial anisotropy is then given by equation (8).

566 Another convenient way to quantify anisotropy is to compute the percentage of  
 567 total anisotropy by taking the L2-norm fraction of the anisotropic part of the elastic  
 568 tensor with respect to the isotropic part. This quantity is called the anisotropy index  
 569 and is given by:

$$570 \quad \text{anisotropy index} = \frac{\|\mathbf{S} - \mathbf{S}_I\|}{\|\mathbf{S}_I\|}. \quad (33)$$

### 571 5 Elastic homogenization of a 2-D mechanically-mixed mantle in the 572 presence of CPO

573 Figure 4 displays some seismic properties of the true elastic structure  $\mathbf{S}$  before  
 574 and after homogenization in a 1000 km  $\times$  1000 km box. The left panels are the  
 575 true structures, whereas the middle and right panels are the structures equating to  
 576 the full effective medium  $\mathcal{H}(\mathbf{S})$  at homogenization wavelengths  $\lambda_h$  of 200 km and  
 577 500 km, respectively. The first row depicts the  $S$ -wave velocities, the second, the  
 578 radial anisotropy, and the third, the anisotropy index. Each pixel initially contains an  
 579 isotropic part derived from the marble cake model with a mixing time for advection  
 580  $T_{\text{SPO}} \sim 75$  My, and an anisotropic part computed from a CPO model with a time  
 581 scale for CPO evolution of  $T_{\text{CPO}} \sim 40$  My corresponding to a moderately developed  
 582 crystal fabric.

583 Several glaring features can be observed such as the presence of positive radial  
 584 anisotropy ( $\xi > 1$ ) at the top and bottom boundaries where flow is sub-horizontal,  
 585 and likewise negative ( $\xi < 1$ ) at regions where the flow is sub-vertical. As expected,  
 586 homogenization results in the smoothing of the structures with the level of smoothing

587 modulated by  $\lambda_h$ . However, homogenization is not just a simple spatial average but  
 588 a product of highly non-linear upscaling relations. With increasing homogenization  
 589 wavelengths, the full effective medium becomes devoid of anisotropy in some areas.

590 After decomposing  $\mathbf{S}$  into an isotropic tensor  $\mathcal{I}(\mathbf{S})$  and an anisotropic tensor  $\mathcal{A}(\mathbf{S})$   
 591 through equations (2) and (4), one can also homogenize and analyze each component  
 592 separately, i.e.  $\mathcal{H}(\mathcal{I}(\mathbf{S}))$  and  $\mathcal{H}(\mathcal{A}(\mathbf{S}))$ . Figure 5 shows the level of effective radial  
 593 anisotropy of these two separate components after homogenization. The top panels  
 594 recreate the results of Alder et al. (2017). Indeed, homogenizing the fine-layered  
 595 isotropic medium produces extrinsic radial anisotropy  $\xi_{\text{SPO}}^*$  (i.e., radial anisotropy of  
 596 model  $\mathcal{H}(\mathcal{I}(\mathbf{S}))$ ). Notice that the patterns of effective intrinsic radial anisotropy and  
 597 extrinsic radial anisotropy maps are roughly similar. For example, they both induce a  
 598 positive radial anisotropy  $\xi > 1$  in the horizontal layers: the stretched heterogeneities  
 599 that induce SPO become elongated along the direction of the maximum principal strain  
 600 rate that also controls the CPO.

601 Figure 6 depicts the apparent isotropic heterogeneities created upon homoge-  
 602 nization of  $\mathcal{A}(\mathbf{S})$ . It produces maximum velocity perturbations of about 0.25 % at  
 603  $\lambda_h = 200$  km and 0.2 % at  $\lambda_h = 500$  km. It appears to be a small effect, especially  
 604 considering the large and sharp variations of intrinsic anisotropy in our CPO model.

605 To better illustrate the behaviour of different contributions to radial anisotropy,  
 606 we plot in Figure 7 the amplitude of radial anisotropy (in terms of its standard de-  
 607 viation over the entire 2-D model domain) against the wavelength of homogenization  
 608  $\lambda_h$ . In the following cases, the intrinsic anisotropy component of  $\mathbf{S}$  is computed for  
 609 a CPO developing over increasing duration  $T_{\text{CPO}}$  of 5, 40, or 75 Myr. Several points  
 610 can be noted in Figure 7:

611 (i) The resulting intrinsic radial anisotropy  $\xi_{\text{CPO}}$  in terms of its standard devi-  
 612 ation over the entire region (dashed lines) increases with  $T_{\text{CPO}}$ , although some sat-  
 613 uration is observed (i.e., the orientation of crystals depends mostly on their recent  
 614 deformation, and lose the memory of the deformation they underwent too long ago).

615 (ii) The level of intrinsic radial anisotropy is diminished upon homogenization.  
 616  $\xi_{\text{CPO}}^*$  (hollow squares) is always lower than the reference value  $\xi_{\text{CPO}}$  (dashed lines), and  
 617 diminishes with  $\lambda_h$ . This effect can be easily understood. For small  $\lambda_h$ , the wavelength

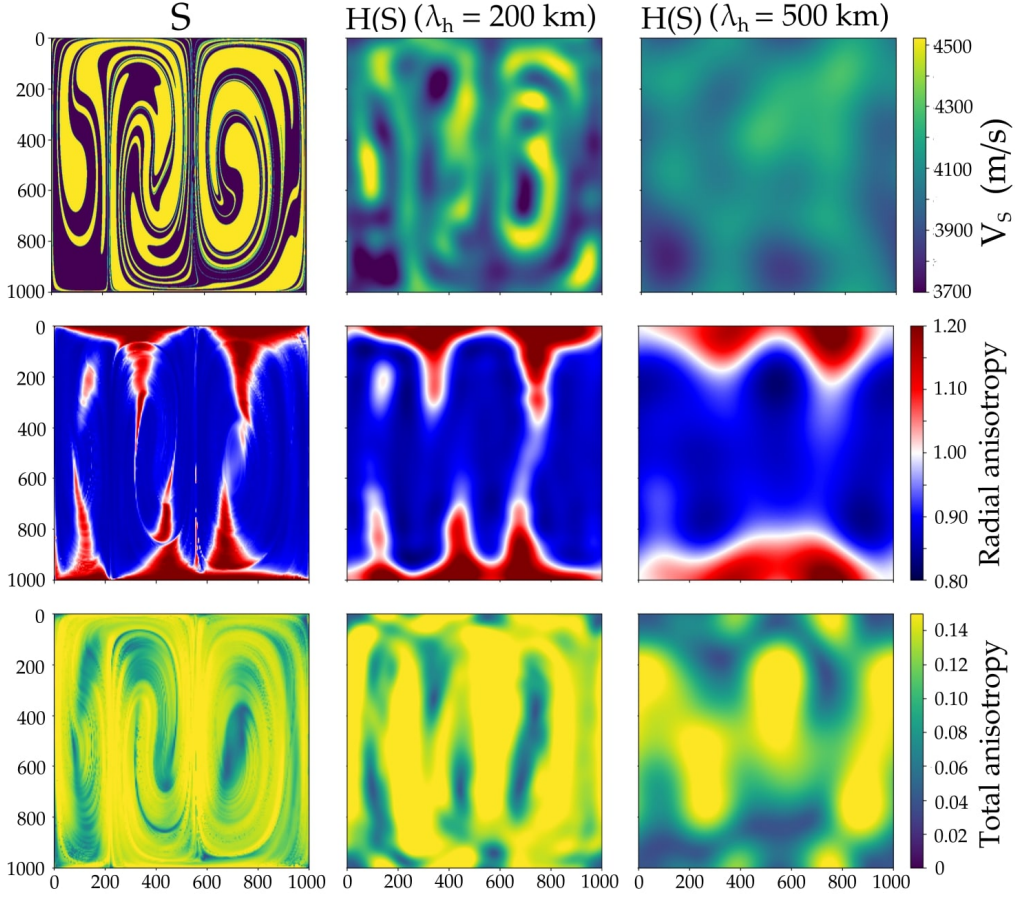


**Figure 4.** Seismic properties of the true elastic structure  $\mathbf{S}$  before and after homogenization. The model dimensions are  $1000 \text{ km} \times 1000 \text{ km}$ . Here, each pixel contains an  $\mathbf{S}$  which consists of small-scale isotropic heterogeneities and an intrinsically anisotropic perturbation computed with D-Rex (Kaminski et al., 2004). The present-day marble cake patterns correspond to a mixing time for advection  $T_{\text{SPO}} \sim 75 \text{ My}$ , whereas the time scale for CPO evolution is  $T_{\text{CPO}} \sim 40 \text{ My}$ . We homogenized  $\mathbf{S}$  using the Fast-Fourier homogenization algorithm of Capdeville et al. (2015). (From left to right) First row:  $V_s$  models derived from  $\mathbf{S}$ ,  $\mathcal{H}(\mathbf{S})$  at  $\lambda_h = 200 \text{ km}$ , and  $\mathcal{H}(\mathbf{S})$  at  $\lambda_h = 500 \text{ km}$ . Second row:  $\xi_{\text{CPO}}$ ,  $\xi^*$  at  $\lambda_h = 200 \text{ km}$ , and  $\xi^*$  at  $\lambda_h = 500 \text{ km}$ . Last row: Total anisotropy in terms of the norm fraction of  $\mathbf{S}$ ,  $\mathcal{H}(\mathbf{S})$  at  $\lambda_h = 200 \text{ km}$ , and  $\mathcal{H}(\mathbf{S})$  at  $\lambda_h = 500 \text{ km}$ . Elastic homogenization can be viewed as the best possible model reconstructed by seismic tomography assuming perfect ray-path coverage.



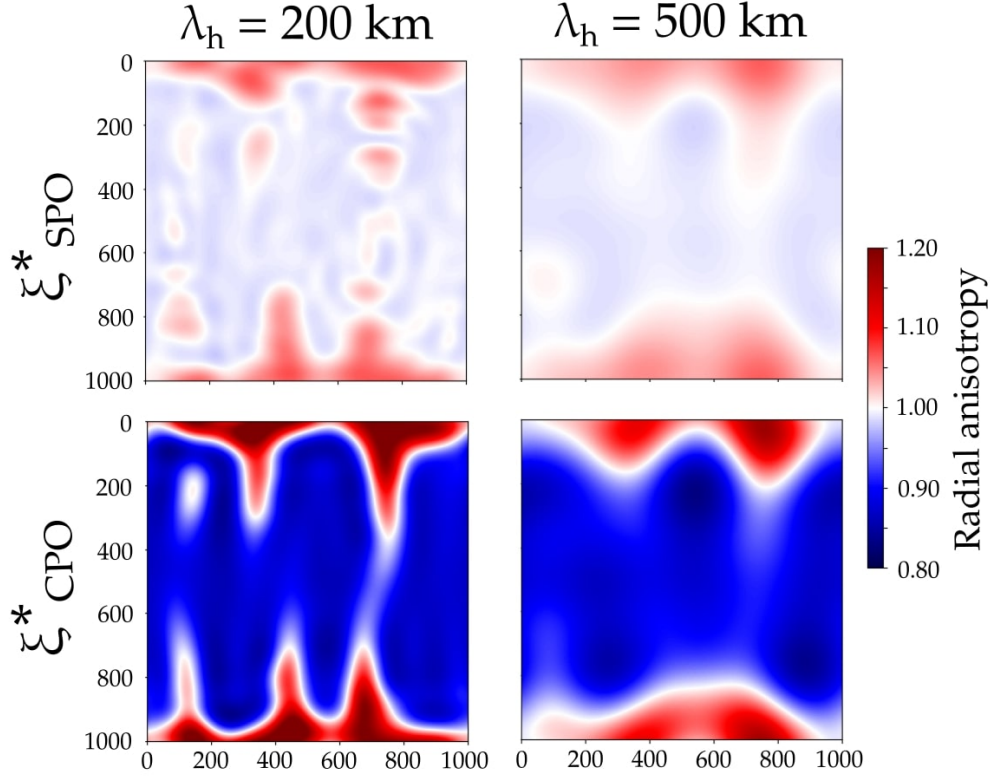


**Figure 5.** Extrinsic radial anisotropy  $\xi_{\text{SPO}}^*$  (*i.e.*, radial anisotropy of model  $\mathcal{H}(\mathcal{I}(\mathbf{S}))$ ) (top panels) at two different wavelengths of homogenization  $\lambda_h$ . It is computed following the projection of the homogenized elastic tensor into an azimuthally-averaged VTI tensor as ‘seen’ by surface waves (Montagner & Nataf, 1986). Here,  $\xi_{\text{SPO}}^* > 1$  is now interpreted as horizontal layering whereas  $< 1$  as vertical layering. The bottom panels show the effective intrinsic radial anisotropy  $\xi_{\text{CPO}}^*$  (*i.e.*, radial anisotropy of model  $\mathcal{H}(\mathcal{A}(\mathbf{S}))$ ).

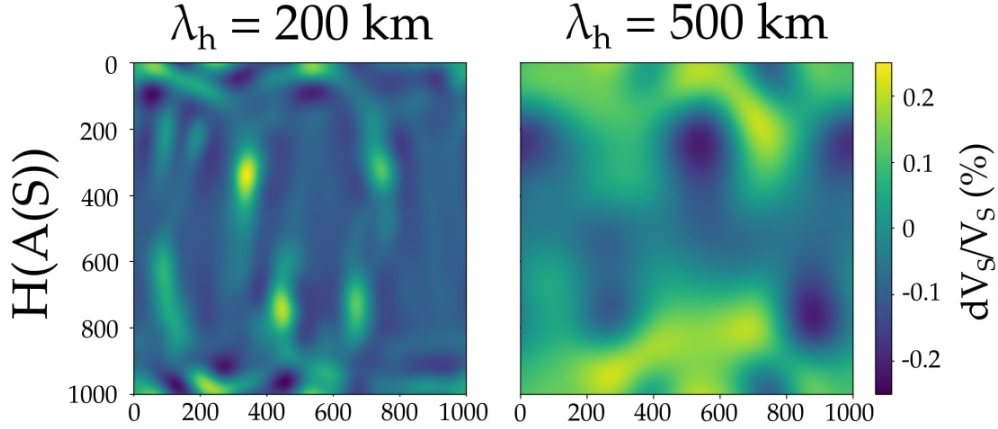


**Figure 6.** Apparent isotropic velocity perturbations with respect to a mean velocity  $V_S$  at two different wavelengths of homogenization  $\lambda_h$ .  $\mathcal{H}(\mathcal{A}(\mathbf{S}))$  pertains to the homogenized model of an anisotropic medium. Even when placed in a very favorable scenario for intrinsic anisotropy, homogenizing an anisotropic medium produces a meager 0.25% artificial heterogeneities at  $\lambda_h = 200$  km and 0.2% at  $\lambda_h = 500$  km.

618 of homogenization is small compared to the scale of deformation patterns (of order 100  
 619 km). At each point of the 2-D map, the direction of CPO is therefore locally constant  
 620 over  $\lambda_h$ , which yields  $\xi_{\text{CPO}}^* \approx \xi_{\text{CPO}}$ . At larger scales, when  $\lambda_h$  increases compared to  
 621 the scale of convection, this direction becomes likely random and CPO heterogeneities  
 622 averaged over  $\lambda_h$  have different orientations: there is less of a preferential direction  
 623 and the averaged level of CPO anisotropy is diminished.

624 (iii) On the contrary, the full effective radial anisotropy  $\xi^*$  at short wavelengths  
 625 of homogenization  $\lambda_h$  is larger than  $\xi_{\text{CPO}}$ . This is in agreement with the analytical  
 626 expression given by equation (22). This additional anisotropy is of course due to  
 627 the existence of SPO (black circles) which reinforces the total level of effective radial  
 628 anisotropy.

629 (iv) Both  $\xi_{\text{CPO}}^*$  and  $\xi^*$  converge toward  $\xi_{\text{CPO}}$  at infinitely short homogenization  
 630 wavelengths. Only in this unrealistic case (*i.e.*, the perfect recording of the seismic  
 631 wavefield up to infinitely short periods), would seismic tomography be able to map the  
 632 true intrinsic radial anisotropy.

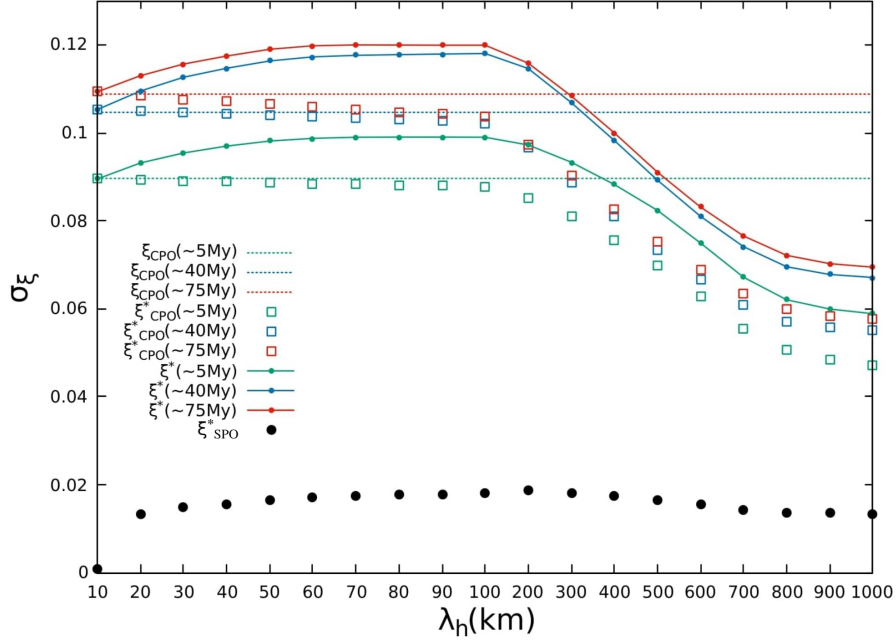


**Figure 7.** Effective radial anisotropy in terms of its standard deviation  $\sigma_\xi$  over the entire 2-D image, plotted as a function of homogenization length. The time scales indicated in million years pertain to the evolution history of CPO (a larger time scale leads to stronger CPO). Dashed lines represent the standard deviation of  $\xi_{\text{CPO}}$  in model **S** and serve as reference values. In this experiment,  $\xi_{\text{SPO}}^*$  of model  $\mathcal{H}(\mathcal{I}(\mathbf{S}))$  (black circles) is deemed to be five times smaller than  $\xi_{\text{CPO}}^*$  of model  $\mathcal{H}(\mathcal{A}(\mathbf{S}))$  (hollow squares). Since SPO is mostly in-phase with CPO, the two anisotropic components add constructively giving the full effective radial anisotropy  $\xi^*$  (solid line-dots).

633 (v) Extrinsic radial anisotropy  $\xi_{\text{SPO}}^*$  here has an amplitude that is five times  
 634 smaller than  $\xi_{\text{CPO}}^*$ . Such a result, of course, is specific to this numerical experiment,  
 635 and that CPO is indeed stronger than SPO might not be always true. For instance, a  
 636 longer mixing time would have resulted in a thinner and more complex layering that  
 637 would have increased the SPO. We are unfortunately limited by the number of tracers  
 638 necessary to describe the phase stirring which is exponentially increasing with time.

### 639 5.1 Verifying the composite law $\xi^* = \xi_{\text{CPO}}^* \times \xi_{\text{SPO}}^*$ in 2-D

640 In this section, we aim to numerically verify equation (28) in 2-D by plotting  $\xi_{\text{SPO}}^*$   
 641  $\times \xi_{\text{CPO}}^*$  against  $\xi^*$  for each pixel in our 2-D maps of radial anisotropy. Here again, the  
 642 three quantities  $\xi_{\text{SPO}}^*$ ,  $\xi_{\text{CPO}}^*$ , and  $\xi^*$  are respectively computed from  $\mathcal{H}(\mathcal{I}(\mathbf{S}))$ ,  $\mathcal{H}(\mathcal{A}(\mathbf{S}))$ ,  
 643 and  $\mathcal{H}(\mathbf{S})$ . We emphasize that since CPO is computed everywhere, there are no CPO  
 644 discontinuities between the yellow and the purple stripes of our 2-D marble cake model;  
 645 the radial anisotropy is almost uniform across thin laminations. Since the cross-term  
 646 in equation (22) depends on small-scales in  $\xi_{\text{CPO}}$ , we expect that there should be  
 647 minimal spatial correlation between CPO and isotropic heterogeneities, and thus the  
 648 effect of the cross-term is effectively mitigated. Figure 8b shows this for two different  
 649 homogenization wavelengths  $\lambda_h$ . We can see that the relation holds exceptionally well  
 650 even for large  $\lambda_h$ .

651 In practice however, tomographic models of  $\xi^*$  are interpreted in terms of intrinsic  
 652 anisotropy, and directly compared with  $\xi_{\text{CPO}}$  computed from CPO models (Becker et  
 653 al., 2003, 2006; Ferreira et al., 2019). We mimic this scenario by comparing  $\xi_{\text{SPO}}^*$   
 654  $\times \xi_{\text{CPO}}$  instead with  $\xi^*$  (Figure 8a). As it turns out, the relation only holds for  
 655 small values of  $\lambda_h$ . At larger values of  $\lambda_h$ , the trend appears to be more dispersed as a  
 656 consequence of the averaging process, losing its viability to some extent. In the absence  
 657 of a homogenized CPO model, we project that this composite law would remain true  
 658 in general under the condition that the minimum wavelength used in tomography is  
 659 sufficiently small.

660 To test the effect of the rigidity-anisotropy cross-term, we consider another man-  
 661 tle model where CPO is only present in one of the two phases of the 2-D marble  
 662 cake illustrated in Figure 3. We impose that the purple component remains isotropic  
 663 and we increase the percentage of isotropic heterogeneities in  $V_S$  to 15%. These two

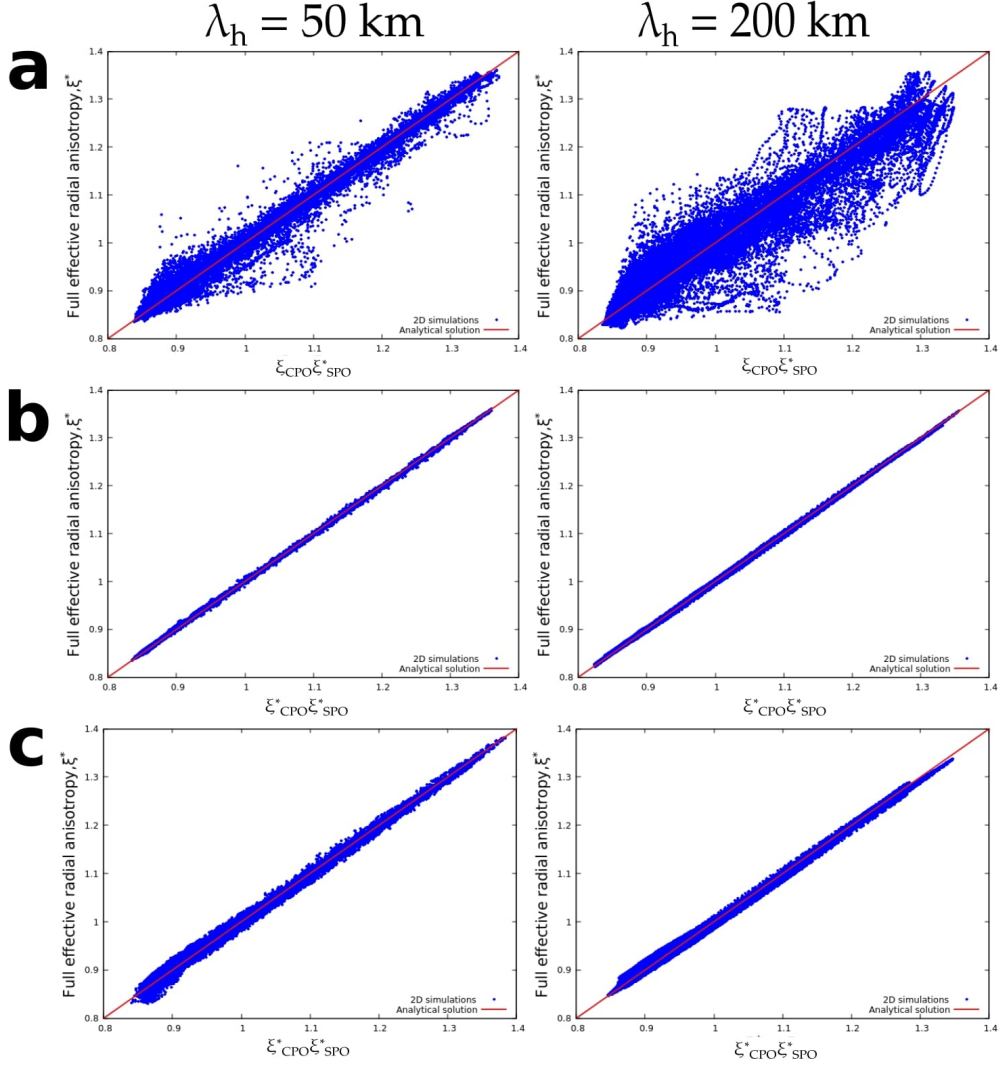


**Figure 8.** Figure 8a: plot of the full effective radial anisotropy  $\xi^*$  as a function of  $\xi_{\text{CPO}} \times \xi_{\text{SPO}}^*$ . CPO is computed everywhere in this case. The media  $\mathbf{S}$  and  $\mathcal{I}(\mathbf{S})$  are homogenized at wavelengths of 50 km (left panel) and 200 km (right panel) to obtain  $\xi^*$  and  $\xi_{\text{SPO}}^*$ , respectively. Figure 8b: the full effective radial anisotropy is now plotted against  $\xi_{\text{CPO}}^* \times \xi_{\text{SPO}}^*$ . The dispersion of the data is immensely reduced when the CPO is homogenized according to equation (28). Figure 8c: the purple phase is now assumed isotropic and the isotropic heterogeneities are increased to 15%. The cross-term, neglected in equation (28), increases moderately the dispersion compared to figure 8b.

664 modifications would increase the correlation between the shear modulus and intrinsic  
 665 radial anisotropy following equation (22). Figure 8c displays the numerical solution at  
 666  $\lambda_h = 50$  km and 200 km when CPO is computed in the yellow phases alone. In this  
 667 scenario, CPO now varies sharply and in the same places as isotropic discontinuities  
 668 (*i.e.*,  $\delta\xi_{\text{CPO}}$  terms in equation (22) are much larger), and as expected the cross-term  
 669 is much more apparent. Nonetheless, this only produces small departures from the  
 670 composite law (red line), implying that the predictions carried out by the composite  
 671 law are robust.

## 672 5.2 Discussion

673 We investigated the effects of elastic homogenization to a specific class of fine-  
 674 scale, marble cake-like models of the mantle in the presence of deformation-induced  
 675 anisotropy. The homogenization procedure can be viewed as a tomographic operator  
 676 applied to a reference elastic model (Capdeville et al., 2013).

677 We showed that the extrinsic radial anisotropy produced by fine-layering could  
 678 reach up to 2% (see Figure 7) assuming 10% of isotropic heterogeneities. This radial  
 679 anisotropy is much lower than the one induced by crystallographic preferred orientation  
 680 (CPO) where the effective intrinsic radial anisotropy could peak at nearly 11%. This  
 681 result is however modulated by some parameters that regulate the level of effective  
 682 radial anisotropy. For example, the layered filaments contrived from our marble cake  
 683 models are of the order 10–100 km whereas of those proposed by Allègre and Turcotte  
 684 (1986) are much thinner and can stretch even further down to the centimeter scale.  
 685 Because heterogeneities in a mechanically-mixed mantle follow a  $1/k$  power spectrum  
 686 (where  $k$  is wavenumber) (Ricard et al., 2014; Mancinelli et al., 2016; Alder et al.,  
 687 2017), meaning that heterogeneities exist at all scales, thinner filaments may induce  
 688 larger extrinsic radial anisotropy by increasing the volume of the mantle where homog-  
 689 enized heterogeneities produce SPO. In addition, effective anisotropy is also affected  
 690 by the level of intrinsic anisotropy. Since CPO results from finite strain accumulation  
 691 over time, the amplitude of intrinsic anisotropy increases with the time scale for CPO  
 692 evolution  $T_{\text{CPO}}$ . Such presumptions may only be valid in regions where rock defor-  
 693 mation varies over extended periods of time, although recrystallization and damage  
 694 would limit the CPO that can be eventually accumulated (Ricard & Bercovici, 2009).  
 695 Furthermore, we considered olivine of type-A crystal fabric as the solitary anisotropic

696 mineral in our mantle models. Because of this, the intrinsic anisotropy produced from  
697 finite deformation should be seen as an upper bound. Inclusion of other anisotropic  
698 minerals such as pyroxene which make up a fraction in mantle periodotite (Maupin  
699 & Park, 2015) would change the net anisotropy. For instance, we anticipate that  
700 including a substantial amount of enstatite would dilute the amount of anisotropy  
701 (e.g. Kaminski et al., 2004). Therefore, whether CPO accounts for most of the bulk  
702 anisotropy observed in tomographic images remains inconclusive and needs further  
703 verification.

704 In light of the simulations conducted, we expect large-scale anisotropy to be only  
705 overestimated when CPO coexists with significant shape preferred orientation (SPO)  
706 as exemplified in our simulations. In the absence of SPO, homogenization can only  
707 decrease the strength of anisotropy. By accounting for both contributions, we showed  
708 that  $\xi > 1$  is attributed to a combination of lateral flow and horizontal layering, and  
709  $\xi < 1$  is a combination of flow ascent and vertical layering. Indeed, the direction of  
710 shear not only dictates the preferred orientation of the anisotropic minerals, but also  
711 of the orientation of the folded strips that gives rise to fine-layering and SPO.

712 The repercussion of homogenizing intrinsic anisotropy alone amounts to the  
713 convection-scale averaging of the CPO as evidenced by our simulations. When  
714 long-period observations sample an intrinsically anisotropic medium, the wavefield  
715 spatially-averages these orientations. As a result, preferential orientations that are  
716 products of imbricated convection tend to appear more heterogeneous, thereby osten-  
717 sibly losing intrinsic anisotropy upon homogenization. In contrast, spatially-coherent  
718 preferential orientations produced by simpler convection patterns are less susceptible  
719 to the dilution of intrinsic anisotropy.

720 The applicability of equation (28) in a 2-D complex media may be of interest  
721 to geodynamicists and tomographers alike. Not only does it permit one to directly  
722 quantify the discrepancy between the full effective radial anisotropy inferred from  
723 a tomographic model and the effective intrinsic radial anisotropy computed from a  
724 homogenized CPO model, it further solidifies the supposition that the mismatch is  
725 indeed a result of extrinsic radial anisotropy due to the seismically-unresolved small-  
726 scale isotropic heterogeneities. We have conducted several numerical experiments to  
727 show that the composite law still holds even when the rigidity-intrinsic anisotropy

728 cross term is amplified. However, the fact that the effect of the cross term is small  
 729 may not be true for all cases, and thus caution must still be undertaken when applying  
 730 the composite law.

731 The conclusions reached in this section are based on a number of simplifying as-  
 732 sumptions: (1) The current forms of the homogenized analytical expressions given by  
 733 equations (22) and (24) neglect  $P$ -wave anisotropy. Our argument was based on how  
 734  $P$ -wave-related structures are poorly constrained by long-period tomography. How-  
 735 ever, Fichtner et al. (2013b) showed that the effective  $S$ -wave radial anisotropy of an  
 736 isotropic-equivalent medium (*i.e.*, fine-layering) also depends on  $P$ -wave anisotropy.  
 737 They concluded that some small-scale isotropic equivalents that give rise to extrin-  
 738 sic anisotropy may be eliminated in the picture if  $P$ -wave anisotropy is known with  
 739 considerable precision. Thus, further developments in our study should address this  
 740 point. (2) We held the isotropic velocity contrast at a fixed value and assumed it to  
 741 be representative of the entire mantle. In reality however,  $V_S$  variations generally de-  
 742 crease with depth (Xu et al., 2008; Stixrude & Jeanloz, 2015). This is not to mention  
 743 the local presence of melt and water that contributes to the variations in wave ve-  
 744 locities, and hence the strength of heterogeneities which completely alters the level of  
 745 apparent anisotropy. (3) We disregarded the dependency of the elastic constants built  
 746 from our mantle models on pressure  $P$  and temperature  $T$ . Future avenues one could  
 747 take would be to incorporate  $P - T$  dependence using empirical relations constrained  
 748 from laboratory experiments. For instance, one may compute  $P - T$  dependence using  
 749 first-order corrections around a reference elastic tensor at ambient  $P - T$  conditions  
 750 (Estey & Douglas, 1986). The availability of self-consistent thermodynamic models  
 751 based on free-energy minimization schemes (J. A. Connolly, 2005; J. Connolly, 2009)  
 752 can also be employed in lieu of the simpler relations for more accurate predictions of  
 753 seismic wave velocities in any given bulk composition (Stixrude & Lithgow-Bertelloni,  
 754 2011).

## 755 **6 Separating SPO from CPO in tomographic models: Application to** 756 **radial anisotropy beneath oceanic plates**

757 Following the verification of the composite law in a 2-D complex medium, in this  
 758 section we present its application to a real-Earth problem. Here, our goal is to assess  
 759 the discrepancy between a tomographic model and a CPO model of upper-mantle



radial anisotropy underneath a mid-ocean ridge. In our hypothesis, this difference should be explained by the extrinsic radial anisotropy due to the unresolved small-scales in seismic velocities.

### 6.1 Radial anisotropy beneath oceanic plates

Within the context of seismic tomography, surface waves offer the capability to image upper-mantle structure providing an in-depth view of large-scale anisotropy (e.g. Rychert et al., 2018). Surface wave tomography images positive radial anisotropy underneath oceanic basins ( $V_{SH} > V_{SV}$ ), characterized by a layer of strong signatures lying in between  $\sim 80 - 200$  km depth, corresponding to the asthenosphere (e.g. Montagner, 1985; Ekström & Dziewonski, 1998; Panning & Romanowicz, 2006; Nettles & Dziewoński, 2008b). The maximum positive vertical gradient of  $\xi^*$ , at  $\sim 80$  km depth, independent of plate age, is a recurrent feature in these tomographic models. This has raised questions about the potential use of radial anisotropy as a marker of the lithosphere-asthenosphere boundary (LAB), which is expected on the contrary to deepen with plate age (Rychert & Shearer, 2011; Burgos et al., 2014; Beghein et al., 2019). The strong radial anisotropy in the asthenosphere is usually explained by geodynamic models including CPO evolution (Becker et al., 2006, 2008).

Across the oceanic lithosphere, plate-averaged radial anisotropy (*i.e.*, all points in the radial anisotropy models with the same plate age are averaged) displays modest levels of about 1–3%. Several models have been proposed to explain these observations. Hansen et al. (2016) and Hedjazian et al. (2017) suggest that CPO-related radial anisotropy developed below the ridge is subsequently frozen in the lithosphere, leading to an age-independent signature. It has also been proposed quasi-laminated melt structures, preserved during lithospheric thickening, can also explain this frozen-in signature of anisotropy (e.g. Auer et al., 2015; Debayle et al., 2020). Hence SPO may also be a potential explanatory mechanism, and a substantial fraction of the observed lithospheric anisotropy may be due to small-scale isotropic heterogeneities (Wang et al., 2013; Kennett & Furumura, 2015).

788

## 6.2 The tomographic model

789

790

791

792

In conjunction with the pre-existing global  $V_{SV}$  model of the upper-mantle constrained from Rayleigh wave data DR2012 (Debayle & Ricard, 2012), we adopt the recent global  $V_{SH}$  model CAM2016SH of Ho et al. (2016) to acquire a plate-averaged 2-D profile of radial anisotropy associated with slow-spreading oceanic ridges.

793

794

795

796

797

The  $V_S$  models were reconstructed by independently inverting Love (for  $V_{SH}$  models) and Rayleigh (for  $V_{SV}$  models) waveforms up to the fifth overtone between the period range 50 – 250 s using an extension of the automated waveform inversion approach of Debayle (1999). We refer the reader to Debayle and Ricard (2012) and Ho et al. (2016) for a more detailed description of the inversion procedure.

798

799

800

801

802

803

From the  $V_{SV}$  and  $V_{SH}$  models of the upper-mantle, we compute the tomographic counterpart of radial anisotropy using  $\xi^* = (V_{SH}/V_{SV})^2$ . Here,  $\xi^*$  is not directly inferred from simultaneous inversions of Love and Rayleigh data but is a rudimentary estimate from the two  $S$ -wave velocity models that may conceivably have different qualities. We view the following exercise as only a proof-of-concept and therefore the results should be interpreted with caution.

804

805

806

807

808

809

810

811

The depth distribution of  $\xi^*$  spanning from 35 – 400 km is shown in Figure 9 (top panel). Positive radial anisotropy values ( $\xi^* > 1$ ) are confined in the upper  $\sim 200$  km of the model domain which is in close agreement with previous studies (e.g. Montagner, 1985; Ekström & Dziewonski, 1998; Panning & Romanowicz, 2006). Although the origin of anisotropy imaged in the asthenosphere is well-understood purely in terms of CPO, anisotropy observed in the lithosphere may be a combination of CPO and SPO (Wang et al., 2013). Here our task is to invoke the composite law to isolate SPO from CPO in this tomographic model with the help of a homogenized CPO model.

812

## 6.3 The CPO model

813

814

815

816

817

In this section, we re-interpret the results of Hedjazian et al. (2017) where they examined radial anisotropy profiles predicted from CPO models produced by plate-driven flows underneath a mid-ocean ridge. From their work, we borrowed two CPO models that correspond to a fast-developing CPO and a slow-developing CPO. The rate is dictated by the dimensionless grain boundary mobility parameter  $M$  which

818 controls the kinetics of grain growth (and hence, the degree of dynamic recrystalliza-  
 819 tion) (Kaminski et al., 2004). In the first case, a value of  $M = 125$  constrained from  
 820 laboratory experiments (Nicolas et al., 1973; Zhang & Karato, 1995) corresponding  
 821 to CPO produced from uniform deformation and initially-random CPO was imposed  
 822 (Kaminski et al., 2004). Subsequently, the second case considers a case where  $M =$   
 823  $10$  (*i.e.*, slower CPO evolution) which also reproduces experimental results but in the  
 824 case of an initially developed CPO (Boneh et al., 2015). We homogenize the two CPO  
 825 models, obtain their long-wavelength effective equivalent, and appraise the resulting  
 826 profiles in comparison with the tomographic model.

### 827 ***6.3.1 The intrinsic CPO mineralogical model***

828 2-D surface-driven mantle flows were acquired using the code `Fluidity` (Davies  
 829 et al., 2011). In both models, upper-mantle deformation is governed by a composite  
 830 dislocation and diffusion creep rheology following the implementation of Garel et al.  
 831 (2014). `D-Rex` was used to model CPO evolution. A complete description of the  
 832 methodology can be found in Hedjazian et al. (2017).

833 Figure 9 displays the intrinsic radial anisotropy profiles  $\xi_{\text{CPO}}$  belonging to the  
 834 fast-evolving CPO with reference `D-Rex` values  $M = 125$  (model A) and the slow-  
 835 evolving CPO with  $M = 10$  (model B). Model A predicts a layer with strong levels  
 836 of intrinsic radial anisotropy of about 10% ( $\xi_{\text{CPO}} \approx 1.1$ ) at a depth of  $\sim 80$  km  
 837 starting at approximately 20 My. At about the same depth, tomographic models  
 838 yield approximately 5% radial anisotropy (e.g. Panning & Romanowicz, 2006; Nettles  
 839 & Dziewoński, 2008b; Burgos et al., 2014). Hence, it has been argued that model A  
 840 overpredicts the observed level of large-scale anisotropy in the upper-mantle (Hedjazian  
 841 et al., 2017). On the contrary, model B predicts modest levels of intrinsic radial  
 842 anisotropy, about 5% ( $\xi_{\text{CPO}} \approx 1.05$ ) across the oceanic lithosphere which is more  
 843 consistent with tomographic observations. In total agreement with Hedjazian et al.  
 844 (2017), these models apparently favor a low grain boundary mobility.

### 845 ***6.3.2 The homogenized CPO model***

846 Figure 9 now shows the effective intrinsic radial anisotropy profiles  $\xi_{\text{CPO}}^*$  of model  
 847  $A^*$  and model  $B^*$ . In both cases, the ensuing patterns of radial anisotropy are smoothed

848 out as a result of homogenization and more so for the fast mobility model A which  
 849 predict a shallow CPO. For instance, the apparent two-layered distribution of intrinsic  
 850 radial anisotropy with depth (down to  $\sim 250$  km) in model A vanishes after homoge-  
 851 nization. The depth profile of effective intrinsic radial anisotropy as a result contain  
 852 one layer of radial anisotropy centered at  $\sim 100$  km depth, making it now compati-  
 853 ble with tomographic models of the asthenosphere. Furthermore, it was inferred that  
 854 radial anisotropy predicted with typical laboratory-derived parameters exceeds tomo-  
 855 graphic observations. Here, we argue that due to finite-frequency effects and eventu-  
 856 ally limitations in resolution power, seismic tomography instead may underestimate  
 857 the strength of intrinsic anisotropy, which further reinforce the need for the presence  
 858 of a non-negligible SPO. As opposed to common practice, the physical parameters  
 859 used in CPO models of which are initially constrained by experimental data may need  
 860 not be manually tuned, and perhaps that the action of varying such parameters to  
 861 conform with tomographic observations deems unnecessary. We therefore conclude  
 862 that direct visual comparison between a CPO model and a tomographic model could  
 863 lead to wrong interpretations, and that homogenization is necessary to have correct  
 864 interpretations of the CPO models.

#### 865 **6.4 Deriving an SPO model**

866 The SPO models of Figure 9 (models C and D) can be estimated by using our  
 867 composite law in equation (28). The extrinsic radial anisotropy is obtained by simply  
 868 dividing the tomographic model of radial anisotropy by that of the homogenized CPO  
 869 model:

$$870 \quad \xi_{\text{SPO}}^* = \frac{\xi^*}{\xi_{\text{CPO}}^*}. \quad (34)$$

871 In this way, models C and D are obtained from models A\* and B\*, respectively.

872 Strong levels of positive extrinsic radial anisotropy near the ridge axis may be  
 873 due to the inability of surface waves to register vertical flow because of its limited  
 874 lateral resolution. Model D, associated with the slow-evolving CPO model B, is almost  
 875 devoid of SPO. This is expected since model B was tailored to fit seismic tomography  
 876 observations from CPO only. Based on our results, one should favor SPO model C  
 877 that corresponds to a fast-evolving CPO model. It displays positive extrinsic radial  
 878 anisotropy above 200 km depth. This is more consistent with the existence of lateral

879 fine-scale structures at the base of the lithosphere (e.g. Auer et al., 2015; Kennett &  
880 Furumura, 2015).

## 881 **7 Conclusion**

882 Differentiating the relative contributions of crystallographic preferred orientation  
883 (CPO) and shape preferred orientation (SPO) to the full effective medium is not a  
884 simple, straightforward process. The tomographic operator (here approximated by  $\mathcal{H}$ )  
885 acts as a smoothing operator, and its inverse is highly non-unique. It is therefore clearly  
886 impossible to separate the CPO and SPO contributions in a tomographic model. One  
887 of the most logical courses of action is to compare tomographic models of anisotropy  
888 with existing micro-mechanical models of CPO evolution (e.g. Becker et al., 2003,  
889 2006; Ferreira et al., 2019). Here, we proposed an approximated composite law that  
890 directly relates the separate contributions of CPO and SPO to the full effective radial  
891 anisotropy  $\xi^*$  inferred from tomographic models:

$$892 \quad \xi^* = \xi_{\text{SPO}}^* \times \xi_{\text{CPO}}^*,$$

893 which we have numerically verified using simple 2-D toy models of an intrinsically  
894 anisotropic and a heterogeneous mantle. Although our numerical experiments were  
895 mainly a proof-of-concept, comparing a CPO model directly to an existing tomographic  
896 model is unwarranted and we highly recommend homogenizing a CPO model as an  
897 intermediate step.

## 898 **Acknowledgments**

899 This work has been funded by the European Union Horizon 2020 research and  
900 innovation programme under grant agreement 716542. The computations were per-  
901 formed using the in-house TRANSCALE cluster situated in Lyon. The texture evo-  
902 lution modeling software, D-Rex (Kaminski et al., 2004), is available at [http://](http://www.ipgp.fr/~kaminski/web_doudoud/DRex.tar.gz)  
903 [www.ipgp.fr/~kaminski/web\\_doudoud/DRex.tar.gz](http://www.ipgp.fr/~kaminski/web_doudoud/DRex.tar.gz). The Fast Fourier Homogeniza-  
904 tion software (Capdeville et al., 2015) can be obtained upon reasonable request to Y.  
905 Capdeville. The tomographic models, DR2012 and CAM2016SH, are described in the  
906 following papers: Debayle and Ricard (2012) and Ho et al. (2016).

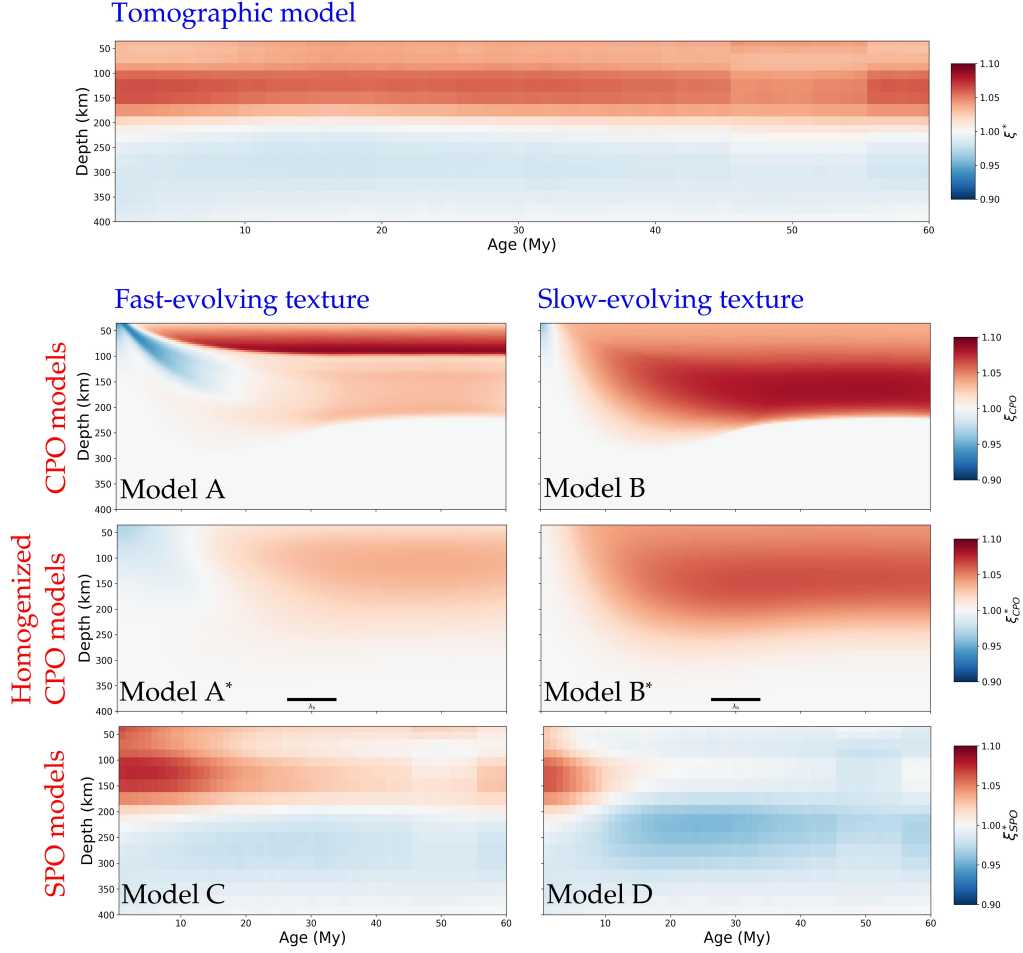


**Figure 9.** Plate-averaged radial anisotropy across the upper-mantle beneath oceanic basins with ages ranging between 0 and 80 Myrs obtained from a tomographic model (top panel), reference CPO models corresponding to fast and slow-evolving textures (models A and B), homogenized versions of model A (model A\*) and of model B (model B\*). The sudden discoloration centered at 50 My in the tomographic model may have resulted from the independent inversions for  $V_{SH}$  and  $V_{SV}$ . This artifact may be eliminated by jointly inverting Love and Rayleigh waveforms for the radial anisotropy instead. Models C and D, respectively, are the extrinsic radial anisotropy profiles computed by dividing  $\xi^*$  of the tomographic model, by  $\xi_{CPO}^*$  of model A\* and B\*, using the composite law. Positive lithospheric radial anisotropy in model C implies the existence of horizontally-laminated structures. This is absent in model D which is expected since model B\* is designed to fit observations.

907 **References**

- 908 Agranier, A., Blichert-Toft, J., Graham, D., Debaille, V., Schiano, P., & Albarède,  
 909 F. (2005). The spectra of isotopic heterogeneities along the mid-atlantic ridge.  
 910 *Earth and Planetary Science Letters*, *238*(1-2), 96–109.
- 911 Alder, C., Bodin, T., Ricard, Y., Capdeville, Y., Debayle, E., & Montagner, J.  
 912 (2017). Quantifying seismic anisotropy induced by small-scale chemical hetero-  
 913 geneities. *Geophysical Journal International*, *211*(3), 1585–1600.
- 914 Allègre, C. J., & Turcotte, D. L. (1986). Implications of a two-component marble-  
 915 cake mantle. *Nature*, *323*(6084), 123–127.
- 916 Auer, L., Becker, T. W., Boschi, L., & Schmerr, N. (2015). Thermal structure,  
 917 radial anisotropy, and dynamics of oceanic boundary layers. *Geophysical Re-  
 918 search Letters*, *42*(22), 9740–9749.
- 919 Backus, G. E. (1962). Long-wave elastic anisotropy produced by horizontal layering.  
 920 *Journal of Geophysical Research*, *67*(11), 4427–4440.
- 921 Bakulin, A. (2003). Intrinsic and layer-induced vertical transverse isotropy. *Geo-  
 922 physics*, *68*(5), 1708–1713.
- 923 Ballmer, M. D., Schmerr, N. C., Nakagawa, T., & Ritsema, J. (2015). Composi-  
 924 tional mantle layering revealed by slab stagnation at  $\sim$  1000-km depth. *Science  
 925 Advances*, *1*(11), e1500815.
- 926 Becker, T. W., Chevrot, S., Schulte-Pelkum, V., & Blackman, D. K. (2006). Statis-  
 927 tical properties of seismic anisotropy predicted by upper mantle geodynamic  
 928 models. *Journal of Geophysical Research: Solid Earth*, *111*(B8).
- 929 Becker, T. W., Kellogg, J. B., Ekström, G., & O’Connell, R. J. (2003). Compari-  
 930 son of azimuthal seismic anisotropy from surface waves and finite strain from  
 931 global mantle-circulation models. *Geophysical Journal International*, *155*(2),  
 932 696–714.
- 933 Becker, T. W., Kustowski, B., & Ekström, G. (2008). Radial seismic anisotropy as  
 934 a constraint for upper mantle rheology. *Earth and Planetary Science Letters*,  
 935 *267*(1-2), 213–227.
- 936 Beghein, C., Snoke, J. A., & Fouch, M. J. (2010). Depth constraints on azimuthal  
 937 anisotropy in the great basin from rayleigh-wave phase velocity maps. *Earth  
 938 and Planetary Science Letters*, *289*(3-4), 467–478.
- 939 Beghein, C., Trampert, J., & Van Heijst, H. (2006). Radial anisotropy in seismic

- 940 reference models of the mantle. *Journal of Geophysical Research: Solid Earth*,  
941 *111*(B2).
- 942 Beghein, C., Xing, Z., & Goes, S. (2019). Thermal nature and resolution of the  
943 lithosphere–asthenosphere boundary under the Pacific from surface waves.  
944 *Geophysical Journal International*, *216*(2), 1441–1465.
- 945 Bodin, T., Capdeville, Y., Romanowicz, B., & Montagner, J. P. (2015). Interpreting  
946 radial anisotropy in global and regional tomographic models. In *The earth's*  
947 *heterogeneous mantle* (pp. 105–144). Springer.
- 948 Boneh, Y., Morales, L. F., Kaminski, E., & Skemer, P. (2015). Modeling olivine  
949 cpo evolution with complex deformation histories: Implications for the in-  
950 terpretation of seismic anisotropy in the mantle. *Geochemistry, Geophysics,*  
951 *Geosystems*, *16*(10), 3436–3455.
- 952 Browaeys, J. T., & Chevrot, S. (2004). Decomposition of the elastic tensor and geo-  
953 physical applications. *Geophysical Journal International*, *159*(2), 667–678.
- 954 Burgos, G., Montagner, J.-P., Beucler, E., Capdeville, Y., Mocquet, A., & Drilleau,  
955 M. (2014). Oceanic lithosphere–asthenosphere boundary from surface wave  
956 dispersion data. *Journal of Geophysical Research: Solid Earth*, *119*(2), 1079–  
957 1093.
- 958 Bystricky, M., Kunze, K., Burlini, L., & Burg, J.-P. (2000). High shear strain of  
959 olivine aggregates: Rheological and seismic consequences. *Science*, *290*(5496),  
960 1564–1567.
- 961 Capdeville, Y., Guillot, L., & Marigo, J.-J. (2010). 2-d non-periodic homogenization  
962 to upscale elastic media for p–sv waves. *Geophysical Journal International*,  
963 *182*(2), 903–922.
- 964 Capdeville, Y., & Marigo, J.-J. (2007). Second order homogenization of the elas-  
965 tic wave equation for non-periodic layered media. *Geophysical Journal Interna-*  
966 *tional*, *170*(2), 823–838.
- 967 Capdeville, Y., & Métivier, L. (2018). Elastic full waveform inversion based on the  
968 homogenization method: theoretical framework and 2-d numerical illustrations.  
969 *Geophysical Journal International*, *213*(2), 1093–1112.
- 970 Capdeville, Y., Stutzmann, E., Wang, N., & Montagner, J. P. (2013). Residual ho-  
971 mogenization for seismic forward and inverse problems in layered media. *Geo-*  
972 *physical Journal International*, *194*(1), 470–487.



- 973 Capdeville, Y., Zhao, M., & Cupillard, P. (2015). Fast fourier homogenization for  
 974 elastic wave propagation in complex media. *Wave Motion*, *54*, 170–186.
- 975 Chang, S.-J., & Ferreira, A. M. (2019). Inference on water content in the mantle  
 976 transition zone near subducted slabs from anisotropy tomography. *Geochem-*  
 977 *istry, Geophysics, Geosystems*, *20*(2), 1189–1201.
- 978 Chen, W.-P., & Brudzinski, M. R. (2003). Seismic anisotropy in the mantle transi-  
 979 tion zone beneath fiji-tonga. *Geophysical Research Letters*, *30*(13).
- 980 Coltice, N., & Ricard, Y. (1999). Geochemical observations and one layer mantle  
 981 convection. *Earth and Planetary Science Letters*, *174*(1-2), 125–137.
- 982 Connolly, J. (2009). The geodynamic equation of state: what and how. *Geochem-*  
 983 *istry, Geophysics, Geosystems*, *10*(10).
- 984 Connolly, J. A. (2005). Computation of phase equilibria by linear programming: a  
 985 tool for geodynamic modeling and its application to subduction zone decarbon-  
 986 ation. *Earth and Planetary Science Letters*, *236*(1-2), 524–541.
- 987 Cowin, S. C., & Mehrabadi, M. M. (1987). On the identification of material symme-  
 988 try for anisotropic elastic materials. *The Quarterly Journal of Mechanics and*  
 989 *Applied Mathematics*, *40*(4), 451–476.
- 990 Crampin, S., & Booth, D. C. (1985). Shear-wave polarizations near the north ana-  
 991 tolian fault–ii. interpretation in terms of crack-induced anisotropy. *Geophysical*  
 992 *Journal International*, *83*(1), 75–92.
- 993 Davies, D. R., Wilson, C. R., & Kramer, S. C. (2011). Fluidity: A fully unstructured  
 994 anisotropic adaptive mesh computational modeling framework for geodynam-  
 995 ics. *Geochemistry, Geophysics, Geosystems*, *12*(6).
- 996 Debayle, E. (1999). Sv-wave azimuthal anisotropy in the australian upper mantle:  
 997 preliminary results from automated rayleigh waveform inversion. *Geophysical*  
 998 *Journal International*, *137*(3), 747–754.
- 999 Debayle, E., Bodin, T., Durand, S., & Ricard, Y. (2020). Seismic evidence for par-  
 1000 tial melt below tectonic plates. *Nature*, *586*(7830), 555–559.
- 1001 Debayle, E., & Kennett, B. (2000). Anisotropy in the australasian upper mantle  
 1002 from love and rayleigh waveform inversion. *Earth and Planetary Science Let-*  
 1003 *ters*, *184*(1), 339–351.
- 1004 Debayle, E., & Ricard, Y. (2012). A global shear velocity model of the upper man-  
 1005 tle from fundamental and higher rayleigh mode measurements. *Journal of Geo-*

- 1006 *physical Research: Solid Earth*, 117(B10).
- 1007 Debayle, E., & Ricard, Y. (2013). Seismic observations of large-scale deformation  
1008 at the bottom of fast-moving plates. *Earth and Planetary Science Letters*, 376,  
1009 165–177.
- 1010 Ekström, G., & Dziewonski, A. M. (1998). The unique anisotropy of the pacific up-  
1011 per mantle. *Nature*, 394(6689), 168–172.
- 1012 Estey, L. H., & Douglas, B. J. (1986). Upper mantle anisotropy: a preliminary  
1013 model. *Journal of Geophysical Research: Solid Earth*, 91(B11), 11393–11406.
- 1014 Faccenda, M., Ferreira, A. M., Tisato, N., Lithgow-Bertelloni, C., Stixrude, L., &  
1015 Pennacchioni, G. (2019). Extrinsic elastic anisotropy in a compositionally  
1016 heterogeneous earth’s mantle. *Journal of Geophysical Research: Solid Earth*,  
1017 124(2), 1671–1687.
- 1018 Ferreira, A. M., Faccenda, M., Sturgeon, W., Chang, S.-J., & Schardong, L. (2019).  
1019 Ubiquitous lower-mantle anisotropy beneath subduction zones. *Nature Geo-*  
1020 *science*, 12(4), 301–306.
- 1021 Fichtner, A., Kennett, B. L., Igel, H., & Bunge, H.-P. (2010). Full waveform to-  
1022 mography for radially anisotropic structure: new insights into present and past  
1023 states of the australasian upper mantle. *Earth and Planetary Science Letters*,  
1024 290(3-4), 270–280.
- 1025 Fichtner, A., Kennett, B. L., & Trampert, J. (2013a). Separating intrinsic and ap-  
1026 parent anisotropy. *Physics of the Earth and Planetary Interiors*, 219, 11–20.
- 1027 Fichtner, A., Kennett, B. L., & Trampert, J. (2013b). Separating intrinsic and ap-  
1028 parent anisotropy. *Physics of the Earth and Planetary Interiors*, 219, 11–20.
- 1029 French, S., Lekic, V., & Romanowicz, B. (2013). Waveform tomography reveals  
1030 channeled flow at the base of the oceanic asthenosphere. *Science*, 342(6155),  
1031 227–230.
- 1032 Friederich, W., & Huang, Z.-X. (1996). Evidence for upper mantle anisotropy be-  
1033 neath southern germany from love and rayleigh wave dispersion. *Geophysical*  
1034 *research letters*, 23(10), 1135–1138.
- 1035 Garel, F., Goes, S., Davies, D., Davies, J. H., Kramer, S. C., & Wilson, C. R.  
1036 (2014). Interaction of subducted slabs with the mantle transition-zone: A  
1037 regime diagram from 2-d thermo-mechanical models with a mobile trench and  
1038 an overriding plate. *Geochemistry, Geophysics, Geosystems*, 15(5), 1739–1765.

- 1039 Guillot, L., Capdeville, Y., & Marigo, J.-J. (2010). 2-d non-periodic homogeniza-  
 1040 tion of the elastic wave equation: Sh case. *Geophysical Journal International*,  
 1041 *182*(3), 1438–1454.
- 1042 Gung, Y., Panning, M., & Romanowicz, B. (2003). Global anisotropy and the thick-  
 1043 ness of continents. *Nature*, *422*(6933), 707–711.
- 1044 Hacker, B. R., Abers, G. A., & Peacock, S. M. (2003). Subduction factory 1. theo-  
 1045 retical mineralogy, densities, seismic wave speeds, and h<sub>2</sub>o contents. *Journal of*  
 1046 *Geophysical Research: Solid Earth*, *108*(B1).
- 1047 Hansen, L. N., Faccenda, M., & Warren, J. M. (2021). A review of mech-  
 1048 anisms generating seismic anisotropy in the upper mantle. *Physics of*  
 1049 *the Earth and Planetary Interiors*, 106662. Retrieved from [https://](https://www.sciencedirect.com/science/article/pii/S0031920121000200)  
 1050 [www.sciencedirect.com/science/article/pii/S0031920121000200](https://www.sciencedirect.com/science/article/pii/S0031920121000200) doi:  
 1051 <https://doi.org/10.1016/j.pepi.2021.106662>
- 1052 Hansen, L. N., Qi, C., & Warren, J. M. (2016). Olivine anisotropy suggests guten-  
 1053 berg discontinuity is not the base of the lithosphere. *Proceedings of the Na-*  
 1054 *tional Academy of Sciences*, *113*(38), 10503–10506.
- 1055 Hedjazian, N., Capdeville, Y., & Thomas, B. (2021). Multiscale seismic imaging  
 1056 with inverse homogenization. *Geophysical Journal International*.
- 1057 Hedjazian, N., Garel, F., Davies, D. R., & Kaminski, E. (2017). Age-independent  
 1058 seismic anisotropy under oceanic plates explained by strain history in the  
 1059 asthenosphere. *Earth and Planetary Science Letters*, *460*, 135–142.
- 1060 Ho, T., Priestley, K., & Debayle, E. (2016). A global horizontal shear velocity model  
 1061 of the upper mantle from multimode love wave measurements. *Geophysical*  
 1062 *journal international*, *207*(1), 542–561.
- 1063 Hofmann, A. W. (1988). Chemical differentiation of the earth: the relationship be-  
 1064 tween mantle, continental crust, and oceanic crust. *Earth and Planetary Sci-*  
 1065 *ence Letters*, *90*(3), 297–314.
- 1066 Kaminski, É., & Ribe, N. M. (2002). Timescales for the evolution of seismic  
 1067 anisotropy in mantle flow. *Geochemistry, Geophysics, Geosystems*, *3*(8), 1–  
 1068 17.
- 1069 Kaminski, É., Ribe, N. M., & Browaeys, J. T. (2004). D-rex, a program for calcu-  
 1070 lation of seismic anisotropy due to crystal lattice preferred orientation in the  
 1071 convective upper mantle. *Geophysical Journal International*, *158*(2), 744–752.

- 1072 Kawakatsu, H., Kumar, P., Takei, Y., Shinohara, M., Kanazawa, T., Araki, E., &  
 1073 Suyehiro, K. (2009). Seismic evidence for sharp lithosphere-asthenosphere  
 1074 boundaries of oceanic plates. *science*, *324*(5926), 499–502.
- 1075 Kendall, J. (2000). Seismic anisotropy in the boundary layers of the mantle. *Earth's*  
 1076 *Deep Interior: Mineral physics and tomography from the atomic to the global*  
 1077 *scale*, *117*, 133–159.
- 1078 Kendall, J., & Silver, P. (1998). Investigating causes of d'' anisotropy. *The core-*  
 1079 *mantle boundary region*, *28*, 97–118.
- 1080 Kennett, B., & Furumura, T. (2015). Toward the reconciliation of seismological and  
 1081 petrological perspectives on oceanic lithosphere heterogeneity. *Geochemistry,*  
 1082 *Geophysics, Geosystems*, *16*(9), 3129–3141.
- 1083 Koelemeijer, P., Ritsema, J., Deuss, A., & Van Heijst, H.-J. (2016). Sp12rts: a  
 1084 degree-12 model of shear-and compressional-wave velocity for earth's mantle.  
 1085 *Geophysical Journal International*, *204*(2), 1024–1039.
- 1086 Kumazawa, M., & Anderson, O. L. (1969). Elastic moduli, pressure derivatives, and  
 1087 temperature derivatives of single-crystal olivine and single-crystal forsterite.  
 1088 *Journal of Geophysical Research*, *74*(25), 5961–5972.
- 1089 Lev, E., & Hager, B. H. (2008). Prediction of anisotropy from flow models: A com-  
 1090 parison of three methods. *Geochemistry, Geophysics, Geosystems*, *9*(7).
- 1091 Long, M. D. (2013). Constraints on subduction geodynamics from seismic  
 1092 anisotropy. *Reviews of Geophysics*, *51*(1), 76–112.
- 1093 Long, M. D., & Becker, T. W. (2010). Mantle dynamics and seismic anisotropy.  
 1094 *Earth and Planetary Science Letters*, *297*(3-4), 341–354.
- 1095 Love, A. E. H. (1906). *A treatise on the mathematical theory of elasticity, by aeh*  
 1096 *love*. The University Press.
- 1097 Mancinelli, N., Shearer, P., & Liu, Q. (2016). Constraints on the heterogeneity spec-  
 1098 trum of earth's upper mantle. *Journal of Geophysical Research: Solid Earth*,  
 1099 *121*(5), 3703–3721.
- 1100 Masters, G., Laske, G., Bolton, H., & Dziewonski, A. (2000). The relative behavior  
 1101 of shear velocity, bulk sound speed, and compressional velocity in the mantle:  
 1102 Implications for chemical and thermal structure. *Earth's deep interior: Mineral*  
 1103 *physics and tomography from the atomic to the global scale*, *117*, 63–87.
- 1104 Masters, T. G., Johnson, S., Laske, G., & Bolton, H. (1996). A shear-velocity

- 1105 model of the mantle. *Philosophical Transactions of the Royal Society of Lon-*  
 1106 *don. Series A: Mathematical, Physical and Engineering Sciences*, 354(1711),  
 1107 1385–1411.
- 1108 Maupin, V., & Park, J. (2015). 1.09—theory and observations—seismic anisotropy.  
 1109 *Treatise on Geophysics*, 277–305.
- 1110 Maupin, V., Park, J., Romanowicz, B., & Dziewonski, A. (2007). Theory and obser-  
 1111 vations—wave propagation in anisotropic media. *Seismology and the Structure*  
 1112 *of the Earth. Treatise on Geophysics*, 1, 289–321.
- 1113 McKenzie, D. (1979). Finite deformation during fluid flow. *Geophysical Journal In-*  
 1114 *ternational*, 58(3), 689–715.
- 1115 McNamara, A. K., van Keken, P. E., & Karato, S. (2002). Development of  
 1116 anisotropic structure by solid-state convection in the earth’s lower mantle.  
 1117 *Nature*, 416(6878), 310–314.
- 1118 Meade, C., Silver, P. G., & Kaneshima, S. (1995). Laboratory and seismological  
 1119 observations of lower mantle isotropy. *Geophysical Research Letters*, 22(10),  
 1120 1293–1296.
- 1121 Montagner, J. P. (1985). Seismic anisotropy of the pacific ocean inferred from long-  
 1122 period surface waves dispersion. *Physics of the earth and planetary interiors*,  
 1123 38(1), 28–50.
- 1124 Montagner, J. P. (2007). Upper mantle structure: Global isotropic and anisotropic  
 1125 elastic tomography. *Treatise on geophysics*, 1, 559–589.
- 1126 Montagner, J.-P., & Jobert, N. (1988). Vectorial tomography—ii. application to the  
 1127 indian ocean. *Geophysical Journal International*, 94(2), 309–344.
- 1128 Montagner, J. P., & Nataf, H. (1988). Vectorial tomography. part i: Theory. *Geo-*  
 1129 *physical Journal International*, 94, 295–307.
- 1130 Montagner, J. P., & Nataf, H.-C. (1986). A simple method for inverting the az-  
 1131 imuthal anisotropy of surface waves. *Journal of Geophysical Research: Solid*  
 1132 *Earth*, 91(B1), 511–520.
- 1133 Moulinec, H., & Suquet, P. (1998). A numerical method for computing the overall  
 1134 response of nonlinear composites with complex microstructure. *Comput. Meth-*  
 1135 *ods Appl. Mech. Engrg.*, 157(1), 69–94.
- 1136 Nettles, M., & Dziewoński, A. M. (2008a). Radially anisotropic shear velocity struc-  
 1137 ture of the upper mantle globally and beneath north america. *Journal of Geo-*

- 1138 *physical Research: Solid Earth*, 113(B2).
- 1139 Nettles, M., & Dziewoński, A. M. (2008b). Radially anisotropic shear velocity struc-  
1140 ture of the upper mantle globally and beneath north america. *Journal of Geo-*  
1141 *physical Research: Solid Earth*, 113(B2).
- 1142 Nicolas, A., Boudier, F., & Boullier, A. (1973). Mechanisms of flow in naturally and  
1143 experimentally deformed peridotites. *American Journal of Science*, 273(10),  
1144 853–876.
- 1145 Nicolas, A., & Christensen, N. I. (1987). Formation of anisotropy in upper mantle  
1146 peridotites-a review. *Composition, structure and dynamics of the lithosphere-*  
1147 *asthenosphere system*, 16, 111–123.
- 1148 Obrebski, M., Kiselev, S., Vinnik, L., & Montagner, J.-P. (2010). Anisotropic strat-  
1149 ification beneath africa from joint inversion of sks and p receiver functions.  
1150 *Journal of Geophysical Research: Solid Earth*, 115(B9).
- 1151 Panning, M., & Romanowicz, B. (2006). A three-dimensional radially anisotropic  
1152 model of shear velocity in the whole mantle. *Geophysical Journal Interna-*  
1153 *tional*, 167(1), 361–379.
- 1154 Plomerová, J., Kouba, D., & Babuška, V. (2002). Mapping the lithosphere–  
1155 asthenosphere boundary through changes in surface-wave anisotropy. *Tectono-*  
1156 *physics*, 358(1-4), 175–185.
- 1157 Press, W. H., Teukolsky, S. A., Flannery, B. P., & Vetterling, W. T. (1992). *Numer-*  
1158 *ical recipes in fortran 77: volume 1, volume 1 of fortran numerical recipes: the*  
1159 *art of scientific computing*. Cambridge university press.
- 1160 Resovsky, J. S., & Ritzwoller, M. H. (1999). A degree 8 mantle shear velocity model  
1161 from normal mode observations below 3 mhz. *Journal of Geophysical Research:*  
1162 *Solid Earth*, 104(B1), 993–1014.
- 1163 Ricard, Y., & Bercovici, D. (2009). A continuum theory of grain size evolution and  
1164 damage. *Journal of Geophysical Research: Solid Earth*, 114(B1).
- 1165 Ricard, Y., Durand, S., Montagner, J.-P., & Chambat, F. (2014). Is there seismic at-  
1166 tenuation in the mantle? *Earth and Planetary Science Letters*, 388, 257–264.
- 1167 Rychert, C. A., Harmon, N., & Tharimena, S. (2018). Seismic imaging of  
1168 the base of the ocean plates. In *Lithospheric discontinuities* (p. 71-  
1169 87). American Geophysical Union (AGU). Retrieved from [https://](https://agupubs.onlinelibrary.wiley.com/doi/abs/10.1002/9781119249740.ch4)  
1170 [agupubs.onlinelibrary.wiley.com/doi/abs/10.1002/9781119249740.ch4](https://agupubs.onlinelibrary.wiley.com/doi/abs/10.1002/9781119249740.ch4)

- 1171 doi: <https://doi.org/10.1002/9781119249740.ch4>
- 1172 Rychert, C. A., & Shearer, P. M. (2011). Imaging the lithosphere-asthenosphere  
1173 boundary beneath the pacific using ss waveform modeling. *Journal of Geophys-*  
1174 *ical Research: Solid Earth*, 116(B7).
- 1175 Sanchez-Palencia, E. (1980). *Non homogeneous media and vibration theory*  
1176 (No. 127). Berlin: Springer.
- 1177 Schlue, J., & Knopoff, L. (1977). Shear-wave polarization anisotropy in the pacific  
1178 basin. *Geophysical Journal International*, 49(1), 145–165.
- 1179 Simmons, N. A., Schuberth, B. S., Myers, S. C., & Knapp, D. R. (2019). Resolution  
1180 and covariance of the llnl-g3d-jps global seismic tomography model: appli-  
1181 cations to travel time uncertainty and tomographic filtering of geodynamic  
1182 models. *Geophysical Journal International*, 217(3), 1543–1557.
- 1183 Stixrude, L., & Jeanloz, R. (2015). Constraints on seismic models from other  
1184 disciplines-constraints from mineral physics on seismological models.
- 1185 Stixrude, L., & Lithgow-Bertelloni, C. (2011). Thermodynamics of mantle minerals-  
1186 ii. phase equilibria. *Geophysical Journal International*, 184(3), 1180–1213.
- 1187 Sturgeon, W., Ferreira, A. M., Faccenda, M., Chang, S.-J., & Schardong, L. (2019).  
1188 On the origin of radial anisotropy near subducted slabs in the midmantle. *Geo-*  
1189 *chemistry, Geophysics, Geosystems*, 20(11), 5105–5125.
- 1190 Takeuchi, H., & Saito, M. (1972). Seismic surface waves. *Methods in computational*  
1191 *physics*, 11, 217–295.
- 1192 Tauzin, B., Bodin, T., Debayle, E., Perrillat, J.-P., & Reynard, B. (2016). Multi-  
1193 mode conversion imaging of the subducted gorda and juan de fuca plates  
1194 below the north american continent. *Earth and Planetary Science Letters*, 440,  
1195 135–146.
- 1196 Tauzin, B., & Ricard, Y. (2014). Seismically deduced thermodynamics phase di-  
1197 agrams for the mantle transition zone. *Earth and Planetary Science Letters*,  
1198 401, 337–346.
- 1199 Thomsen, L. (1986). Weak elastic anisotropy. *Geophysics*, 51(10), 1954–1966.
- 1200 Tkalčić, H., Pasyanos, M. E., Rodgers, A. J., Gök, R., Walter, W., & Al-Amri, A.  
1201 (2006). A multistep approach for joint modeling of surface wave dispersion  
1202 and teleseismic receiver functions: Implications for lithospheric structure of the  
1203 arabian peninsula. *Journal of Geophysical Research: Solid Earth*, 111(B11).

- 1204 Tommasi, A., Mainprice, D., Canova, G., & Chastel, Y. (2000). Viscoplastic self-  
1205 consistent and equilibrium-based modeling of olivine lattice preferred orien-  
1206 tations: Implications for the upper mantle seismic anisotropy. *Journal of*  
1207 *Geophysical Research: Solid Earth*, 105(B4), 7893–7908.
- 1208 Trampert, J., & van Heijst, H. J. (2002). Global azimuthal anisotropy in the transi-  
1209 tion zone. *Science*, 296(5571), 1297–1299.
- 1210 Wang, N., Montagner, J. P., Fichtner, A., & Capdeville, Y. (2013). Intrinsic versus  
1211 extrinsic seismic anisotropy: The radial anisotropy in reference earth models.  
1212 *Geophysical Research Letters*, 40(16), 4284–4288.
- 1213 Wookey, J., & Kendall, J.-M. (2004). Evidence of midmantle anisotropy from shear  
1214 wave splitting and the influence of shear-coupled p waves. *Journal of Geophys-*  
1215 *ical Research: Solid Earth*, 109(B7).
- 1216 Xie, J., Ritzwoller, M. H., Shen, W., & Wang, W. (2017). Crustal anisotropy across  
1217 eastern tibet and surroundings modeled as a depth-dependent tilted hexago-  
1218 nally symmetric medium. *Geophysical Journal International*, 209(1), 466–491.
- 1219 Xie, J., Ritzwoller, M. H., Shen, W., Yang, Y., Zheng, Y., & Zhou, L. (2013).  
1220 Crustal radial anisotropy across eastern tibet and the western yangtze craton.  
1221 *Journal of Geophysical Research: Solid Earth*, 118(8), 4226–4252.
- 1222 Xu, W., Lithgow-Bertelloni, C., Stixrude, L., & Ritsema, J. (2008). The effect of  
1223 bulk composition and temperature on mantle seismic structure. *Earth and*  
1224 *Planetary Science Letters*, 275(1-2), 70–79.
- 1225 Zhang, S., & Karato, S.-i. (1995). Lattice preferred orientation of olivine aggregates  
1226 deformed in simple shear. *Nature*, 375(6534), 774.